

# The P-wave velocity and azimuthal anisotropy structure of southeastern margin of the Tibetan Plateau from adjoint-state traveltimes tomography

Xuezhen ZHANG<sup>1</sup>, Xiaodong SONG<sup>1\*</sup>, Jing CHEN<sup>2</sup>, Lei ZHANG<sup>1</sup>, Ping TONG<sup>2</sup> & Yan'e LI<sup>3</sup>

<sup>1</sup> State Key Laboratory of Deep Earth and Mineral Exploration, School of Earth and Space Sciences, Peking University, Beijing 100871, China

<sup>2</sup> Division of Mathematical Sciences, School of Physical and Mathematical Sciences, Nanyang Technological University, Singapore 637371, Singapore

<sup>3</sup> Institute of Geophysics, China Earthquake Administration, Beijing 100081, China

Received July 5, 2024; revised December 2, 2024; accepted December 25, 2024; published online February 14, 2025

**Abstract** The southeastern margin of the Tibetan Plateau is a crucial region to understand the mechanisms of plateau uplift and deformation. This region is seismically active and has experienced multiple large earthquakes, resulting in significant human and economic losses. Constructing velocity and anisotropic tomography models is crucial for understanding the seismogenic mechanism and deep structural deformation in this area. In this study, we extract high-quality P-wave first-arrival data from the earthquake catalog of the China Earthquake Administration and use them to construct both common-receiver and common-source differential traveltimes datasets. We then apply a novel adjoint-state traveltimes tomography approach to obtain new P-wave velocity and azimuthal anisotropy models for the region. This method eliminates the need for ray tracing, thereby reducing the potential bias from the ray theory and ray tracing. A comparison between our results and previous imaging models and shear-wave splitting measurements reveals several new details. The results indicate weak anisotropy in the shallow depth of the central Chuandian block. Two low-velocity anomalies are identified beneath the Songpan-Ganzi and Lijiang-Xiaojinhe fault zones, as well as beneath the Xiaojiang Fault. The distinct anisotropic characteristics of these two low-velocity anomalies suggest different tectonic contexts: Beneath the Songpan-Ganzi and Lijiang-Xiaojinhe fault zones, the azimuthal anisotropy aligns north-south and northeast-southwest, while beneath the Xiaojiang Fault, it aligns northwest-southeast. In addition, the anisotropy of the upper mantle in the southern part of the study area has a significant east-west feature. The earthquake relocation results reveal intensified seismic activity in regions with significant velocity contrasts and near fault zones. Segmental seismic activity is observed along some major fault zones, and seismicity is also more pronounced in fault intersection areas. The new imaging results provide new perspectives and insights for understanding the seismogenic mechanisms and regional tectonic deformation in the region.

**Keywords** Azimuthal anisotropy, P-wave velocity, Adjoint-state tomography, Tibetan Plateau, Sichuan and Yunnan

**Citation:** Zhang X, Song X, Chen J, Zhang L, Tong P, Li Y. 2025. The P-wave velocity and azimuthal anisotropy structure of southeastern margin of the Tibetan Plateau from adjoint-state traveltimes tomography. *Science China Earth Sciences*, 68(3): 702–719, <https://doi.org/10.1007/s11430-024-1504-x>

## 1. Introduction

The Tibetan Plateau has undergone intense compressional

folding and significant crustal shortening due to the collision between the Indian and Eurasian plates over the past 50 Ma (e.g., Molnar and Tapponnier, 1975; Yin and Harrison, 2000; Tapponnier et al., 2001; Kind et al., 2002; Royden et al., 2008; Burchfiel and Chen, 2013; Ding et al., 2022). This

\* Corresponding author (email: [xiao.d.song@gmail.com](mailto:xiao.d.song@gmail.com))

geological evolution has resulted in a surface uplift of over 4 km and crustal thickening to about 80 km (Schoenbohm et al., 2006; Royden et al., 2008; Wang C et al., 2014). Previous studies have proposed various models to explain the mechanism of the large-scale uplift and geodynamic process of the Tibetan Plateau, including the rigid block extrusion model (Molnar and Tapponnier, 1975; Peltzer and Tapponnier, 1988; Tapponnier et al., 1982, 2001), continuous deformation model (England and Houseman, 1986, 1988), and mid-lower crustal flow model (e.g., Royden et al., 1997, 2008; Clark and Royden, 2000; Beaumont et al., 2001; Copley and McKenzie, 2007). Nevertheless, increasing geophysical evidence suggests that widespread crustal flow may not exist within the Tibetan Plateau, but may be confined to localized regions (e.g., Bai et al., 2010). The rigid block extrusion model also inadequately explains the internal movement of the blocks. Thus, there remains ongoing debate regarding the mechanisms and geodynamic processes for the uplift of the Tibetan Plateau.

The southeastern margin of the Tibetan Plateau serves as a critical window for understanding the uplift mechanisms as the materials from the Tibetan Plateau have escaped and extruded in the southeast direction (Figure 1; Tapponnier et al., 2001; Burchfiel and Chen, 2013; Wang et al., 2015; Huang et al., 2021; Hou et al., 2024). Surface GPS measurements show a clockwise movement of materials around the eastern structural segment of the Tibetan Plateau (Figure

1b; Shen et al., 2005; Rui and Stamps, 2019; Wang and Shen, 2020). The southeastern margin comprises several blocks (Figure 1), including the rigid Sichuan Basin (SCB), Songpan-Ganzi Terrain (SGT), Yangtze Craton (YZC), Chuandian rhombic block (CDT), Cathaysia Fold Belt (CFB), and Indo-China Block (ICB). The region is characterized by a few main active faults (Figure 1; Deng et al., 2003; Zhang, 2013), such as the Longmenshan Fault (LMSF), the Xianshuihe Fault (XSHF), the Xiaojiang Fault (XJF), and the Red River Fault (RRF). The Emeishan large igneous province (ELIP) is located in the central part of CDT, inferred to have formed approximately 250 Ma during the Late Permian mantle plume eruption (Xu et al., 2004, 2007; Ali et al., 2005; Shellnutt, 2014). The interactions between these blocks and fault systems contribute to the complex crustal deformation mechanisms in this region. The southeastern margin of the Tibetan Plateau is one of the most seismically active regions in the world, having experienced numerous earthquakes with magnitudes greater than 6 (e.g. the 2008  $M_S$  8.0 Wenchuan earthquake and the 2013  $M_S$  7.0 Lushan earthquake), resulting in significant human and economic losses. Therefore, tomographic studies of the velocity and anisotropic structure of this region are crucial for understanding the ground motions, seismic mechanisms, and earthquake prevention and disaster reduction.

Seismic velocity structure provides constraints about the composition, temperature, partial melting of the earth med-

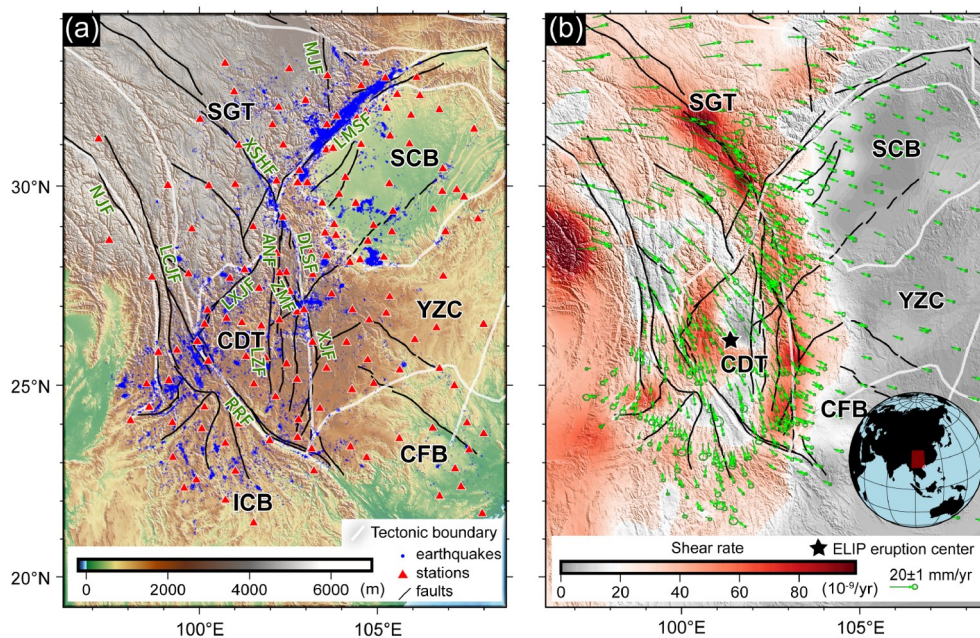


**Figure 1** Tectonic map and geodetic displacement and strain of the study region. (a) Tectonic unit and main active faults (modified from Deng et al., 2003; Liang et al., 2004; Zhang, 2013; Xin et al., 2019) with the distribution of the earthquakes (blue dots) and stations (red triangles) used in the study. (b) Surface GPS displacement measurements (from Wang and Shen, 2020) and the maximum shear strain rate (from Rui and Stamps, 2019). The study region is highlighted in red zone on the global map in the lower right corner. CDT, Chuandian Terrain; CFB, Cathaysia Fold Belt; ELIP, Emeishan large igneous province; ICB, Indo-China Block; SCB, Sichuan Basin; SGT, Songpan-Ganzi Terrain; YZC, Yangtze Craton. ANF, Anninghe Fault; DLSF, Daliangshan Fault; LCJF, Lancangjiang Fault; LMSF, Longmengshan Fault; LXJF, Lijiang-Xiaojinhe Fault; LZJF, Lüzhijiang Fault; NJF, Nujiang Fault; MJF, Minjiang Fault; RRF, Red River Fault; XJF, Xiaojiang Fault; XSHF, Xianshuihe Fault; ZMF, Zemuhe Fault.

ium (Boyd et al., 2004). Seismic anisotropic structure may imply existing fractures, subsurface material movement, and potential stress-strain fields (e.g., Crampin et al., 1984; Weiss et al., 1999; Boness and Zoback, 2006; Fouch and Rondenay, 2006; Zhao et al., 2016; Huang et al., 2018). Despite ongoing controversy about the causes of anisotropy, the two main candidates are currently the shape-preferred orientation (SPO) and lattice-preferred orientation (LPO) of the Earth's medium (e.g., Crampin et al., 1984; Weiss et al., 1999; Montagner and Guillot, 2002; Wenk, 2002; Fouch and Rondenay, 2006). In 2018, China Seismic Experimental Site (CSES) was established in the southeastern margin of the Tibetan Plateau (Wu and Li, 2021). In the past few decades, numerous studies have developed various velocity and anisotropic models about this region. Many isotropic velocity models have been obtained from surface wave tomography from ambient noise or earthquake (e.g., Yao et al., 2006, 2008; Yang et al., 2012; Qiao et al., 2018; Li L et al., 2021), body wave traveltome tomography (e.g., Huang et al., 2003, 2012; Huang et al., 2015; Hua et al., 2018; Wei and Zhao, 2022; Hu et al., 2024; Wu et al., 2024), full waveform inversion (e.g., Chen et al., 2015; Dong et al., 2019; Xiao et al., 2020), and joint inversion of different data (e.g., Liu et al., 2014; Bao et al., 2015; Feng et al., 2020; Liu Y et al., 2021, 2023; Hou et al., 2024). Anisotropic measurements beneath the stations at the southeast Tibetan Plateau have been derived from local earthquakes shear-wave splitting (e.g., Shi et al., 2012, 2013; Zhang and Gao, 2017; Zhang et al., 2018; Gao et al., 2020), teleseismic SKS, SKKS, PKS splitting (e.g., Sol et al., 2007; Shi et al., 2012; Chang et al., 2015; Kong et al., 2018; Huang and Chevrot, 2021), and receiver function (e.g., Hu et al., 2018; Zheng et al., 2018; Han et al., 2020; Peng et al., 2022). Furthermore, many studies have developed the three-dimensional anisotropic models from Rayleigh wave anisotropic tomography (e.g., Yao et al., 2010; Liu et al., 2019; Bao et al., 2020; Cao et al., 2020; Liang et al., 2020; Dong and Yang, 2022; Han et al., 2022; Zhang Z et al., 2023), P-wave anisotropic tomography (e.g., Wei et al., 2013; Huang et al., 2018; Liu et al., 2022), and Pn-wave anisotropic tomography (e.g., Liang and Song, 2006; Lü et al., 2011; Lei et al., 2014; Du et al., 2019; Nie et al., 2021).

Presently, most of the traveltome tomography for velocity and anisotropic structure is based on ray tracing (e.g., Zhang and Thurber, 2003, 2006; Huang et al., 2018; Han et al., 2021; Liu et al., 2023). However, the accurate determination of the ray paths within the highly heterogeneous anisotropic structures is challenging (Rawlinson et al., 2008; Liu and Tong, 2021; Tong, 2021a). To avoid potential errors associated with ray tracing and to utilize the prevalent adjoint method, Tong (2021a, 2021b) developed a novel traveltome inversion method for velocity and azimuthal anisotropic structure based on the eikonal equation. This method elim-

inates the need for ray tracing to update the model. Instead, it employs the adjoint method to compute sensitivity kernels for model update. In this study, we select the first arrival time data from the catalog of the China Earthquake Administration. By applying the new traveltome tomography, we obtain the new P-wave velocity and azimuthal anisotropic models for the southeastern margin of the Tibetan Plateau. Our finding provides the new perspectives and understanding of the deformation and seismogenic mechanisms of the crust and upper mantle in the southeast Tibetan Plateau.

## 2. Data

We apply strict selection criteria to the earthquake catalog from 2008 to 2022 achieved in the China Earthquake Administration. Specifically, we initially perform the regression analysis on the raw traveltome dataset. Then, we delete arrival times far away from the main trend (greater than 2.75 s) in the raw dataset, and discard earthquakes with less than 7 records. Consequently, we obtain 38,661 events and 498,848 P-wave arrival time data (Figure 1a; Figure 2a, 2b; Appendix Figure S1, <https://link.springer.com>), referred to as absolute traveltome (ABS) data. Furthermore, about 5,635,364 common-receiver differential traveltome (CR) data are extracted by limiting the maximum separation of earthquake pairs to 10 km, and 649,754 common-source differential traveltome (CS) data are extracted based on the common-source ray azimuth angle less than 30°.

## 3. Methodology

We adopt the novel Adjoint-state traveltome tomography (referred as “TomoATT”; Tong, 2021a, 2021b) to obtain the crustal P-wave velocity and the azimuthal anisotropic structure using absolute and differential traveltome data. The comprehensive description of the method is presented in Tong (2021a, 2021b), Tong et al. (2023), and Chen et al. (2023a). TomoATT has several advantages, including reliance on the eikonal equation without ray tracing, incorporation of surface topography, consideration of Earth's curvature, partial resolution of multipath issues, and efficient and accurate computation of the traveltome field. The following provides a concise overview of the method and the inversion workflow in this study.

### 3.1 Adjoint-state traveltome tomography for azimuthal anisotropic media

The traveltome field  $T(\mathbf{x})$  of the wavefront in an azimuthal anisotropic medium is governed by the eikonal equation with

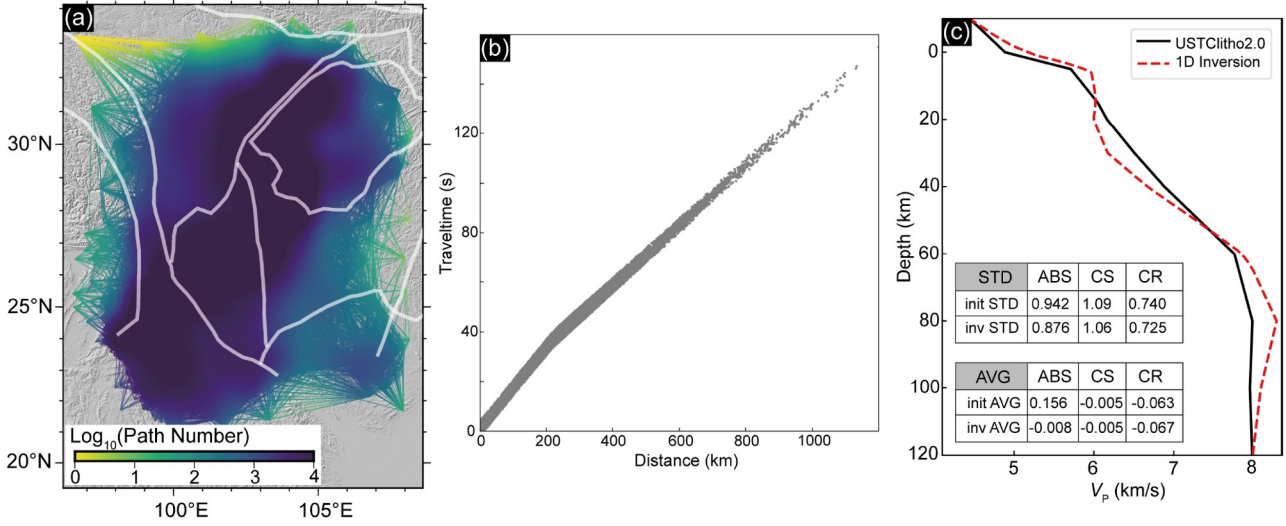


**Figure 2** Distribution of data coverage, traveltime-distance scatter plot, and one-dimensional average  $V_p$  model. (a) Spatial distribution and density of the great circle paths associated with traveltime data. (b) Traveltime-distance scatter plot of the selected data used in the inversion. (c) Results of the one-dimensional  $V_p$  model inversion along with the summary table of average (AVG, in s) and standard deviation (STD, in s) of residuals before and after inversion. Black line indicates the 1D average model of USTClitho2.0 (Han et al., 2021) in our study region.

a point-source  $\mathbf{x}_s$  condition

$$\begin{cases} \sqrt{[\nabla T(\mathbf{x})]^t \mathbf{M}(\mathbf{x}) \nabla T(\mathbf{x})} = 1, & \mathbf{x} \in \Omega \setminus \{\mathbf{x}_s\} \\ T(\mathbf{x}_s) = 0, \end{cases} \quad (1)$$

where  $\Omega$  is the Earth's volume and  $\mathbf{x}_s$  is the source location. The spherical coordinates  $\mathbf{x} = (r, \theta, \phi)$  are considered, where  $r$ ,  $\theta$  and  $\phi$  represent the distance to the Earth center, latitude, and longitude, respectively. The symmetric positive definite matrix  $\mathbf{M}(\mathbf{x})$ , as detailed in Luo and Qian (2012), Tong (2021b), describes the anisotropic medium. In order to reducing the number of unknown, TomoATT only consider three model parameters  $\zeta(\mathbf{x}), \eta(\mathbf{x}), s(\mathbf{x})$ . Here  $s(\mathbf{x})$  is azimuthally average slowness, while  $\zeta(\mathbf{x})$  and  $\eta(\mathbf{x})$  server as azimuthally anisotropic parameters describing the anisotropic magnitude  $\epsilon(\mathbf{x}) = \sqrt{\zeta^2(\mathbf{x}) + \eta^2(\mathbf{x})}$ , and the clockwise angle  $\psi(\mathbf{x}) = \frac{1}{2} \arctan\left(\frac{\eta(\mathbf{x})}{\zeta(\mathbf{x})}\right)$  between the fast velocity direction and the east direction (Chen et al., 2023a). The matrix  $\mathbf{M}(\mathbf{x})$  can be represented as

$$\mathbf{M}(\mathbf{x}) = \frac{1}{s^2(\mathbf{x})} \begin{pmatrix} 1 & 0 & 0 \\ 0 & 1 - 2\zeta(\mathbf{x}) & 2\eta(\mathbf{x}) \\ 0 & 2\eta(\mathbf{x}) & 1 + 2\zeta(\mathbf{x}) \end{pmatrix}. \quad (2)$$

TomoATT aims at determining the optimal parameters that minimize the overall misfit between the observed and predicted traveltimes and differential traveltimes, given by  $\min_{s, \zeta, \eta} \chi(s, \zeta, \eta) = \chi_{\text{abs}}(s, \zeta, \eta) + \chi_{\text{cs}}(s, \zeta, \eta) + \chi_{\text{cr}}(s, \zeta, \eta)$ , (3) where the misfits of ABS, CS, and CR data are separately written as

$$\chi_{\text{abs}}(s, \zeta, \eta) = \sum_{n=1}^{N_s} \sum_{m=1}^{N_r} \frac{w_{n,m}}{2} [T_n^{\text{pred}}(\mathbf{x}_{r,m}) - T_{n,m}^{\text{obs}}]^2, \quad (4)$$

$$\chi_{\text{cs}}(s, \zeta, \eta) = \sum_{n=1}^{N_s} \sum_{k=1}^{N_r} \sum_{m=1}^{N_r} \frac{w_{n,mk}}{2} \cdot [ (T_n^{\text{pred}}(\mathbf{x}_{r,m}) - T_n^{\text{pred}}(\mathbf{x}_{r,k})) - (T_{n,m}^{\text{obs}} - T_{n,k}^{\text{obs}}) ]^2, \quad (5)$$

$$\chi_{\text{cr}}(s, \zeta, \eta) = \sum_{n=1}^{N_s} \sum_{j=1}^{N_s} \sum_{m=1}^{N_r} \frac{w_{nj,m}}{2} \cdot [ (T_n^{\text{pred}}(\mathbf{x}_{r,m}) - T_j^{\text{pred}}(\mathbf{x}_{r,m})) - (T_{n,m}^{\text{obs}} - T_{j,m}^{\text{obs}}) ]^2. \quad (6)$$

where  $T_{n,m}^{\text{obs}}$  is the observed traveltime originating from the  $n$ -th source at  $\mathbf{x}_{r,m}$  and recorded by the  $m$ -th receiver at  $\mathbf{x}_{r,m}$ . Correspondingly,  $T_n^{\text{pred}}(\mathbf{x}_{r,m})$  is the synthetic traveltime governed by eq. (1). And the  $w_{n,m}, w_{n,mk}, w_{nj,m}$  are the weights of data depending on the quality and the density of traveltime data.

TomoATT employs adjoint method to determinate the sensitive kernels of traveltime data misfit with respect to the model parameters (see Figure 3 for an example of the individual sensitive kernels with respect to the slowness of the ABS, CS, and CR data, separately). After obtaining the sensitivity kernels, TomoATT employs the step-size controlled gradient descent method to simultaneously update the P-wave velocity and azimuthal anisotropic models in an iterative manner (Chen et al., 2023a, 2023b). The multiple-grid model parameterization (Tong et al., 2019; Tong, 2021a) is applied to mitigate the influence of subjective inversion grid selection, enhancing the robustness of inversion. Considering the uneven distribution of data, TomoATT performs

appropriate normalization according to the density of sensitive kernels. Additionally, TomoATT also possesses the capability to relocate earthquakes during the iteration (Tong et al., 2023) like the practice of many tomography studies (e.g., Zhang and Thurber, 2003, 2006; Han et al., 2021; Liu et al., 2023). It is noteworthy that the earthquakes relocation also considers the influence of anisotropy, improving forward modeling and therefore location accuracy.

### 3.2 Inversion strategy and model parameterization

Three types of data constrain model and earthquake location with different emphasis. ABS data is sensitive to the absolute seismic velocity and earthquake location (Figure 3b). CS data emphasizes the receiver-side structure, and reduces the effect of source uncertainty (including the uncertainty of hypocenter location and origin time) on model inversion (Figure 3c; e.g., Yuan et al., 2016; Chen et al., 2023; Tong et al., 2023). CR data, by reducing the uncertainty of receiver-side structures (Figure 3d), has been proven effective for earthquake relocation (e.g., Waldhauser and Ellsworth, 2000; Zhang and Thurber, 2003; Allam and Ben-Zion, 2012; Tong et al., 2023). Therefore, in this study, ABS and CS data are used for the inversion of  $V_p$  velocity and azimuthal anisotropy structure, while earthquake relocation incorporates ABS and CR data.

The inversion process is divided into two stages. First, we perform a one-dimensional (1D) velocity inversion based on the ABS data. It starts with a 1D model of the horizontal average of the USTCL2.0 model within the study region (Figure 2c, black curve). The resulting final 1D model (Figure 2c, red dashed lines) serves as the initial model for the subsequent 3D inversion of the isotropic velocity model and the azimuthal anisotropy model and reference model in the checkerboard resolution tests. We then perform two parallel 3D model inversions: one that inverts only the isotropic P-wave velocity and another that simultaneously inverts both the anisotropic P-wave velocity and the azimuthal anisotropy. The initial iterations of the inversion are performed on a coarse grid, followed by further iterations on a finer grid. The grid configurations are shown in supplementary Figures S2 and S3.

## 4. 1D velocity inversion and checkerboard resolution tests

### 4.1 1D model

The 1D velocity model inversion reduces the initial residual mean of the ABS data from approximately 0.156 s to about 0 s (Figure 2c), indicating the 1D model is not underestimated and overestimated. The STD of residuals decreases from 0.942 to 0.876 s (Figure 2c). As the initial model for the

subsequent 3D inversion, it effectively eliminates systematic biases from the data. The 1D velocity model shows overall similar trends with the 1D average model of the UST-Clitho2.0 (Han et al., 2021) in our study region (Figure 2c). However, there is noticeable decrease in the velocity gradient near 20 km depth, followed by a significant increase in the velocity gradient near 50 km depth. At about 80 km depth, our 1D velocity model is slightly higher than that of the USTClitho2.0.

### 4.2 Assessment of resolution capability

The checkerboard resolution test provides a reference for the resolution of the tomography model and is commonly employed, although it may have certain limitations (Lévêque et al., 1993; Liang et al., 2004; Rawlinson and Spakman, 2016). Refer to Zelt (1998), Liang et al. (2004) and Huang et al. (2015), we define two indicators to quantify the resolutions of velocity and anisotropy in the checkerboard test.

$$R_{\text{vel}}(\mathbf{x}) = \frac{\int_{\theta-h}^{\theta+h} \int_{\phi-h}^{\phi+h} (c(\mathbf{x}) + c_r(\mathbf{x}))^2 r^2 \cos\theta d\theta d\phi}{2 \int_{\theta-h}^{\theta+h} \int_{\phi-h}^{\phi+h} (c(\mathbf{x})^2 + c_r(\mathbf{x})^2) r^2 \cos\theta d\theta d\phi}, \quad (7)$$

$$R_{\text{azi}}(\mathbf{x}) = \frac{\int_{\theta-h}^{\theta+h} \int_{\phi-h}^{\phi+h} (\epsilon_T(\mathbf{x}) + \epsilon(\mathbf{x}) \cos(\psi(\mathbf{x}) - \psi_T(\mathbf{x})))^2 r^2 \cos\theta d\theta d\phi}{2 \int_{\theta-h}^{\theta+h} \int_{\phi-h}^{\phi+h} (\epsilon(\mathbf{x})^2 + \epsilon_T(\mathbf{x})^2) r^2 \cos\theta d\theta d\phi}, \quad (8)$$

where  $(c, \epsilon, \psi)$  are recovered velocity and azimuthal anisotropy parameters, and  $(c_T, \epsilon_T, \psi_T)$  are true model parameters. In this test, we select  $h=1^\circ$ . Empirically, we regard the areas where  $R>0.7$  as well-recover domain in the checkerboard test (Zelt, 1998; Liang et al., 2004).

### 4.3 Resolution test of isotropic $V_p$ model inversion

We perform a checkerboard resolution test to evaluate the inversion of the isotropic velocity model. We assign staggered  $\pm 5\%$  velocity perturbations to the 1D output model (Figure 2c, red dashed lines), constructing the checkerboard model. In the depth range of 0–20 km, the size of velocity anomalies in depth and lateral direction is approximately  $10 \text{ km} \times 0.7^\circ \times 0.7^\circ$ . In the depth range of 20–30 km, the anomaly size is about  $10 \text{ km} \times 0.9^\circ \times 0.9^\circ$ . At the depth of 30–45 km, the anomaly size is about  $15 \text{ km} \times 1.1^\circ \times 1.1^\circ$ , and at greater depths, the anomaly size is around  $20 \text{ km} \times 1.5^\circ \times 1.5^\circ$  (Figure S4). The configuration of dataset is consistent with that of real-data inversion. To simulate the noise of the real data, we add Gaussian noise with a mean of 0 s and a standard deviation of 0.1 s to the ABS data. Similarly, the CS and CR data are constructed using the same approach applied to process the real data.

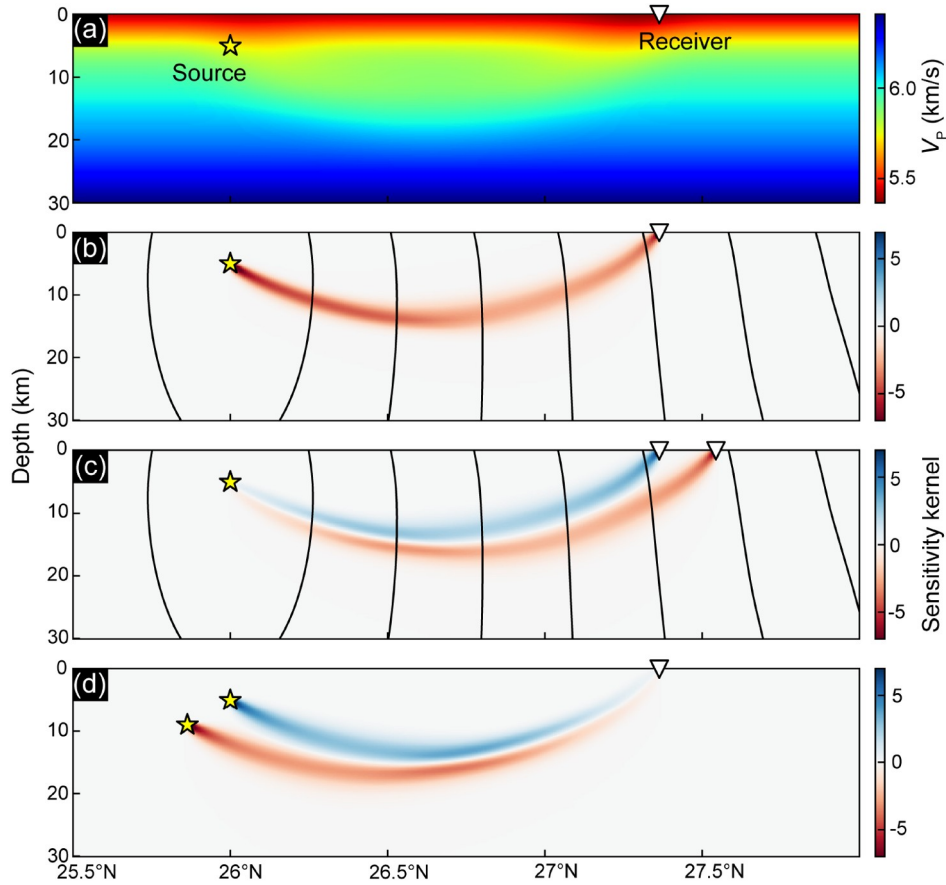


**Figure 3** The sensitivity kernels of three types of traveltime data. (a) An example velocity model used to compute sensitivity kernels with respect to the traveltime misfit. (b)–(d) are sensitivity kernels between the sources and receivers of ABS data, CS data, and CR data, respectively. The solid curves in (b) and (c) are traveltime isochrones at an interval of 5 s.

The results of the resolution test suggest that the isotropic inversion show relatively high resolution in regions with good data coverage (Figure 4; Figure S5). The standard deviation (STD) of the data residuals after inversion is close to the STD of the noise (Figure 4f). In both shallow and deep depths (5, 15, 37, and 55 km), the checkerboard model can be well recovered in most areas within our study region. At 25 km depth, the recovery of the checkerboard model is less effective in the northwestern and southeastern parts of the study region, possibly due to the limited rays of the first-arriving P-wave data (Xu and Song, 2010).

#### 4.4 Resolution test of azimuthal anisotropic model inversion

We introduced staggered  $\pm 5\%$  velocity perturbations and 5% anisotropy magnitude perturbations with two fast velocity directions ( $60^\circ$  and  $150^\circ$ ) to the 1D inversion model to construct the checkerboard model for azimuthal anisotropy inversion. The noise in ABS data and construction of the CS and CR data are the same as those used in isotropic checkerboard resolution test. Considering the increased inversion

parameters in the anisotropic inversion, the size of velocity anomalies in the checkerboard model is slightly larger than that in the isotropic checkerboard model. Moreover, the size of the azimuthal anisotropy anomalies is slightly larger than the velocity anomalies. At depths of 0–20 km, the size of velocity anomalies in the depth and lateral directions is approximately  $10 \text{ km} \times 1^\circ \times 1^\circ$ , while the size of anisotropic anomalies is  $10 \text{ km} \times 1.5^\circ \times 1.5^\circ$ . At depths of 20–40 km, the size of velocity anomalies is about  $20 \text{ km} \times 1.2^\circ \times 1.2^\circ$ , and the size of anisotropic anomalies is  $20 \text{ km} \times 1.6^\circ \times 1.6^\circ$ . At deeper depths, the size of velocity anomalies is about  $20 \text{ km} \times 1.5^\circ \times 1.5^\circ$ , and the size of anisotropic anomalies is about  $20 \text{ km} \times 1.7^\circ \times 1.7^\circ$  (Figure S6; Figure 6). From the inversion results (Figure 5; Figure 6), it can be observed that azimuthal anisotropy and seismic velocity in the central part of the study area can be effectively recovered. The STD of the residuals after inversion is also close to the STD of the noise level (Figure 5e). In addition, we perform a leakage test to assess the degree of coupling between the velocity structure and the azimuthal anisotropy. Using the same parameter settings as in the previous inversion, we design a checkerboard model with only velocity anomalies, excluding ani-

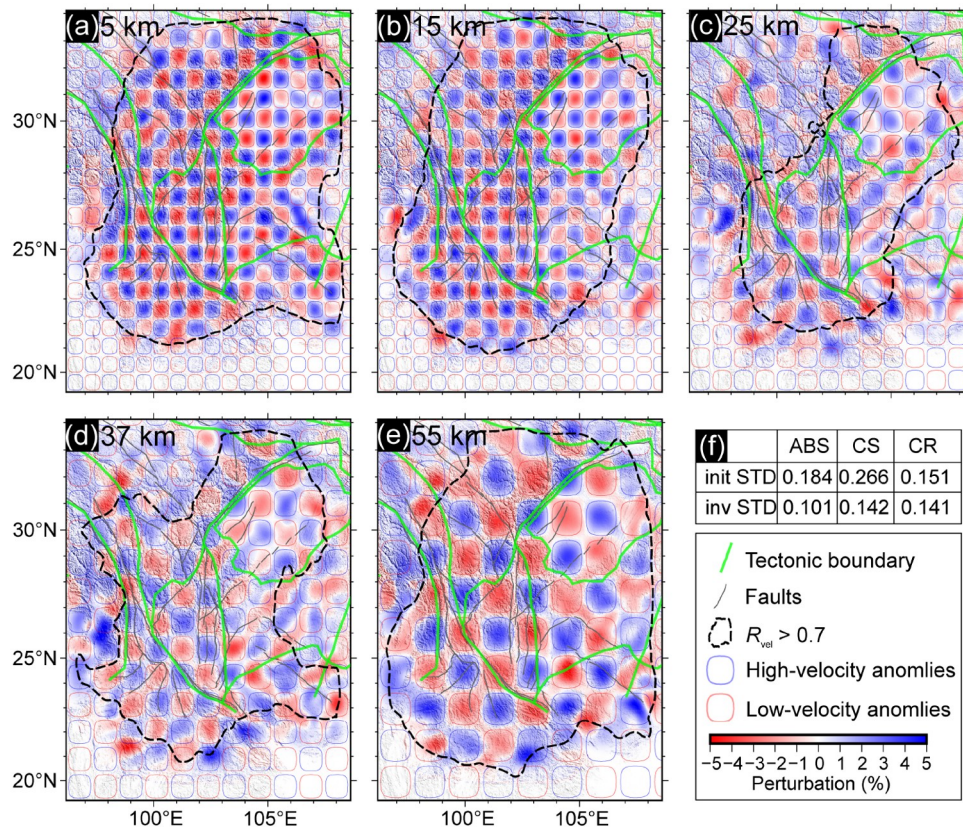


**Figure 4** Results of the isotropic checkerboard resolution test at five depths. (a)–(e) Show the results at five depths, respectively. (f) Summary table showing the STD of the traveltime residuals for the three types of data before and after inversion. The region within the black dashed lines is regarded to be well-resolved ( $R_{\text{vel}}(\mathbf{x}) > 0.7$ ) (Figure S5). The blue and red contours indicate the locations of the high- and low-velocity perturbations in the checkerboard model, respectively.

sotropy, and then invert for both velocity and anisotropy structures simultaneously. The results show that the anisotropy structure is scarcely recovered (see Figure S7), indicating that the data used in this study can effectively decouple velocity and anisotropy. Therefore, the tomographic model presented in this study is relatively reliable.

## 5. Tomographic results

### 5.1 Isotropic $V_p$ structure

Our isotropic velocity inversion effectively reduces the STD of data residuals (Figure 7a–7c). The STD of ABS data residuals decrease from 0.88 s to about 0.49 s, with a reduction of approximately 44%. Similarly, the STD of the CR data residuals decrease from 0.73 s to about 0.40 s, approximately a 45% decrease. The STD of CS data residuals decrease from 1.06 to 0.73 s, a reduction of about 31%. This significant decreases in residuals STD suggest a substantial improvement in data fit.

We present the perturbation maps of tomographic models relative to average velocity at given depths (Figure 8), and the maps of the absolute velocity of tomographic models are

shown in Figure S9. The earthquake relocation results are shown in Figure S10. Our findings reveal significant low-velocity anomalies beneath the SCB in the shallow depth (5 km, Figure 8), likely associated with the extensive sedimentary layers in the area (Liu S et al., 2021; Wang et al., 2021; Xia et al., 2021). In particular, at a depth of 15 km (Figure 8), a low velocity anomaly appears on the periphery of the CDT, mainly beneath the LXJF and XJF. In contrast, a pronounced high-velocity anomaly is observed in the central part of the CDT, extending northeastward beneath the SCB. At a depth of 25 km, this high-velocity anomaly appears to be surrounded by low-velocity bodies. At depths of 37 and 55 km (Figure 8), the velocity features in the model are relatively simple, with the distribution of high- and low-velocity anomalies within the CDT largely corresponding to Moho depth variations (Dong et al., 2020; Cheng et al., 2022).

### 5.2 Azimuthal anisotropic structure

The azimuthal anisotropic inversion results in a more reduction in data residuals compared to isotropic inversion due to the additional inversion parameters for anisotropic mod-

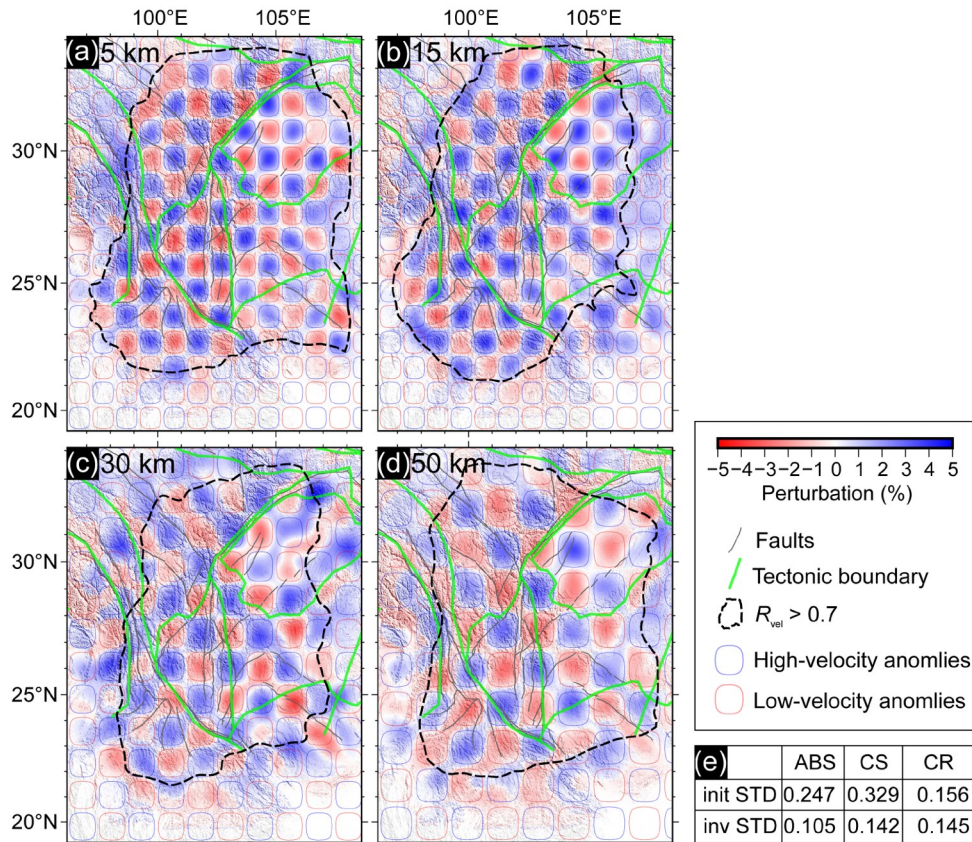


**Figure 5**  $V_p$  results of the checkerboard resolution test for the P-wave azimuthal anisotropy. (a)–(d) Show the results at four depths, respectively. (e) Summary table showing the STD of the traveltime residuals for the three types of data before and after inversion. The region within the black dashed lines is regarded to be well-resolved ( $R_{vel}(x) > 0.7$ ) (Figure S8a–S8d). The blue and red contours indicate the locations of the high- and low-velocity perturbations in the checkerboard model, respectively.

eling. The STD of residuals for ABS, CS, and CR data decreases by approximately 47%, 45%, and 33%, respectively (Figure 7d–7f). Figure 9 shows the anisotropic velocity and azimuthal anisotropic structure in the well-resolution region, determined by the intersection of the regions with well-recovered velocity and azimuthal anisotropy from the checkerboard resolution test (Figures 5 and 6). The earthquake relocation results are shown in Figure S11.

From the perspective of anisotropic  $V_p$  velocity structure (Figure 9), at shallow depths (5 km, Figure 9a), the anisotropic velocity structure closely resembles to the isotropic results. Both exhibit low-velocity anomalies beneath the SCB and the eastern margin of the Tibetan Plateau, while the southern part of the study area shows relatively high velocities. At 15 km depth (Figure 9b), there are low-velocity anomalies in the SGT, LXJF, and the western part of YZC. By a depth of 30 km (Figure 9c), prominent low-velocity anomalies are observed beneath SGT, LXJF, and XJF, while high-velocity anomalies are primarily located beneath the SCB and the southern side of RRF. The central part of the CDT exhibits less distinct high-velocity features. At 50 km depth (Figure 9d), the patterns of high and low velocities

show a good agreement with the variation of Moho depth (Cheng et al., 2022).

From the perspective of azimuthal anisotropy structure (Figure 9), at shallow depths (5 and 15 km; Figure 9a, 9b), the fast-velocity direction (FVD) is predominantly aligned with the surface GPS and the strike of active faults. In the SGT region, the FVDs have a northwest-southeast orientation. Near LXJF, there is a certain angle between the FVDs and the strike of LXJF. At RRF and LCJF, the FVDs are well-aligned with the fault orientation. Similarly, at XJF and LZJF, the FVDs also show good consistency with the strike-slip faults. However, in the central part of CDT, there is a weak azimuthal anisotropy feature, consistent with the findings of Li et al. (2020) and Han et al. (2022). At a depth of 30 km (Figure 9c), the overall FVDs are generally consistent with the surface GPS directions. Between SGT and ICB, the FVDs shift from northwest-southeast to north-south, and then transition to northeast-southwest, indicating a pronounced clockwise trend. The low-velocity anomaly beneath the LXJF has a north-south or northeast-southwest FVD, whereas the low-velocity anomaly beneath the XJF has a northwest-southeast FVD. These two regions have almost

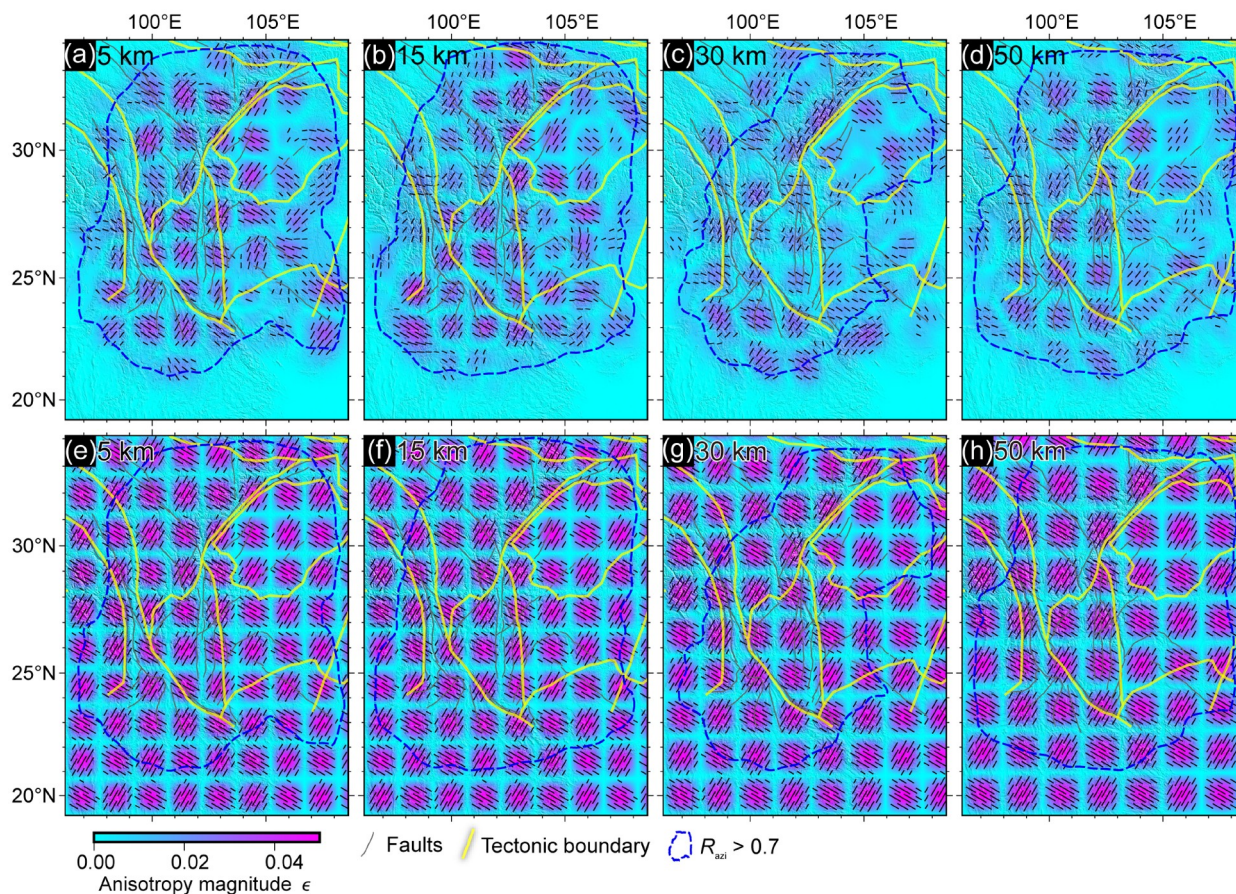


**Figure 6** Azimuthally anisotropic results of the checkerboard resolution test for the P-wave azimuthal anisotropy and the checkerboard model. (a)–(d) Show the results at four depths, respectively. (e)–(h) Show the checkerboard model at the same four depths, respectively. The region within the black dashed lines is regarded to be well-resolved ( $R_{azi}(\mathbf{x}) > 0.7$ ) (Figure S8e–S8h). The color indicates the magnitude of anisotropy.

perpendicular anisotropy directions. The differences in anisotropic structure suggest that these areas may be within different tectonic settings. At a depth of 50 km (Figure 9d), a prominent feature is that, south of 26°N, the overall FVDs tend to be east-west, while the FVDs in SGT and CDT tend to be north-south.

## 6. Discussions

### 6.1 Model comparison with previous studies

We compare our isotropic P-wave velocity model with the community velocity model in southwestern China (CVM2.0; Liu et al., 2023) and the recently developed velocity model of the lithospheric continental of China (USTClitho2.0; Han et al., 2021). Both CVM2.0 and USTClitho2.0 are developed using ray tracing methods and considering the topography of the Earth. The 1D average velocity in our model is similar to the CVM2.0 at depth of 5–25 km (Figure 7g). However, at deeper depths, our model shows slower velocities compared to both CVM2.0 and USTClitho2.0. Following Zhang et al. (2022, 2023), we calculate the correlation coefficient be-

tween the perturbation patterns of our model and those of CVM2.0/USTClitho2.0. At the depths of 5 and 15 km (Figure 7h), the correlation coefficients between the models are relatively low. The previous tomographic model comparison studies (Zhang X et al., 2022, 2023; Huang et al., 2024) also observe the significant differences at the shallow depths, attributed to the complexity of shallow structures and variations in parameter settings during the inversion. The overall structure of our model is generally consistent with the CVM2.0 and USTClitho2.0 models, showing a low velocity anomaly beneath the SCB at 5 km depth, extensive low velocity anomalies at 15 and 25 km depth, and distinct high and low velocity patterns at 37 and 55 km depth (Figures 8 and S9). However, differences are observed in the distribution of low-velocity anomalies beneath the LXJF and the XJF at 25 km depth. Our model suggests that the low-velocity regions in these areas are continuous, in close agreement with the results of Hu et al. (2024), whereas the CVM2.0 and USTClitho2.0 models suggest that these low-velocity anomalies are separated. These model discrepancies are likely due to several factors. Both our study and Hu (2024) rely solely on P-wave arrival data, whereas CVM2.0 and

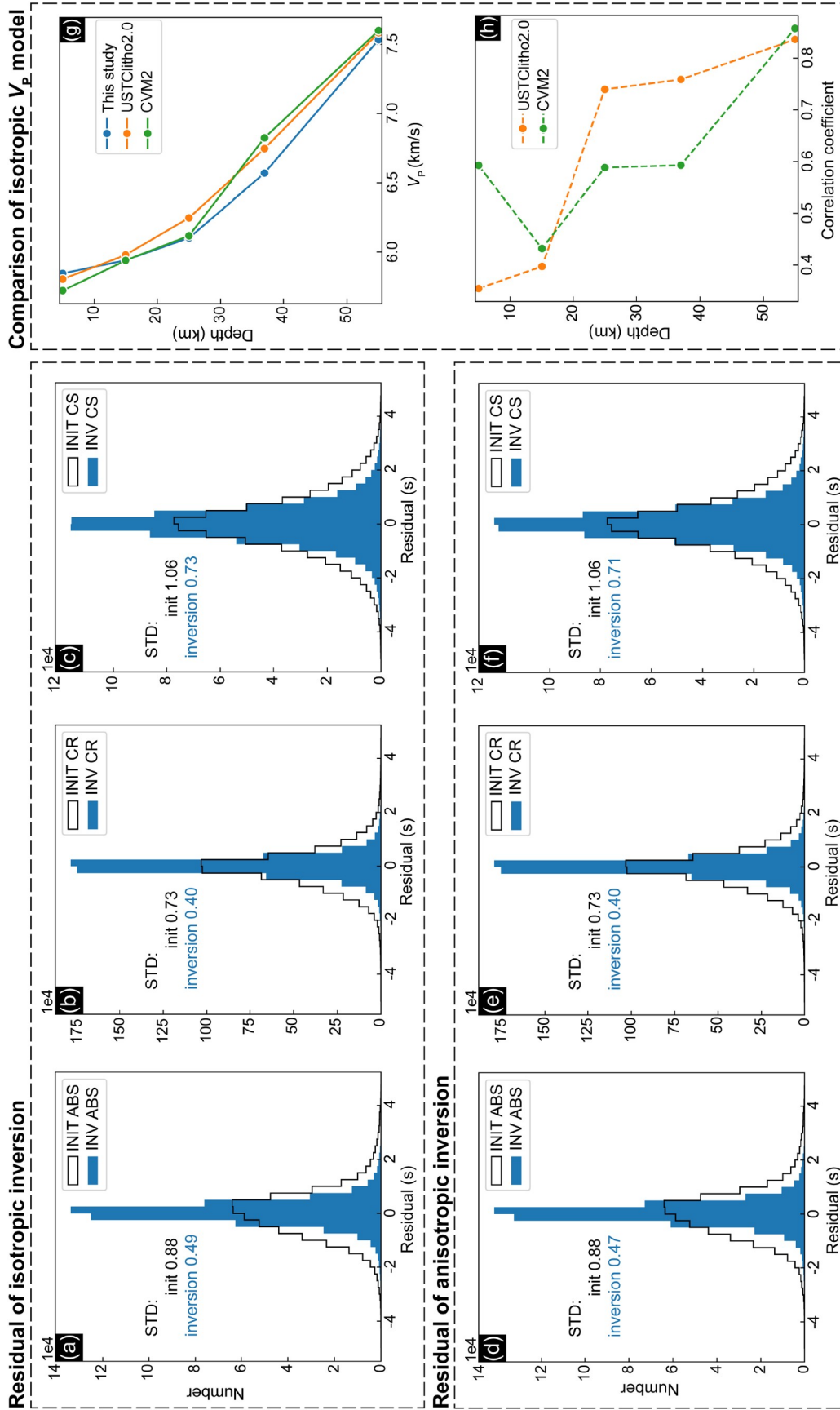


**Figure 7** Residual statistics for isotropic and anisotropic inversions and the isotropic  $V_p$  model comparison. (a)–(c) are histograms of residuals before (black line) and after (filled in blue) isotropic inversion with labeled STDs for ABS data, CR data, and CS data, respectively. (d)–(f) are histograms of residuals before (black line) and after (filled in blue) anisotropic inversion with labeled STDs for ABS data, CR data, and CS data, respectively. (g) 1D average  $V_p$  model comparison between our isotropic inverted model and USTClitho2.0 (Han et al., 2021) and CVM2.0 (Liu et al., 2023). (h) Correlation coefficients between our isotropic inverted model and USTClitho2.0 and CVM2.0.

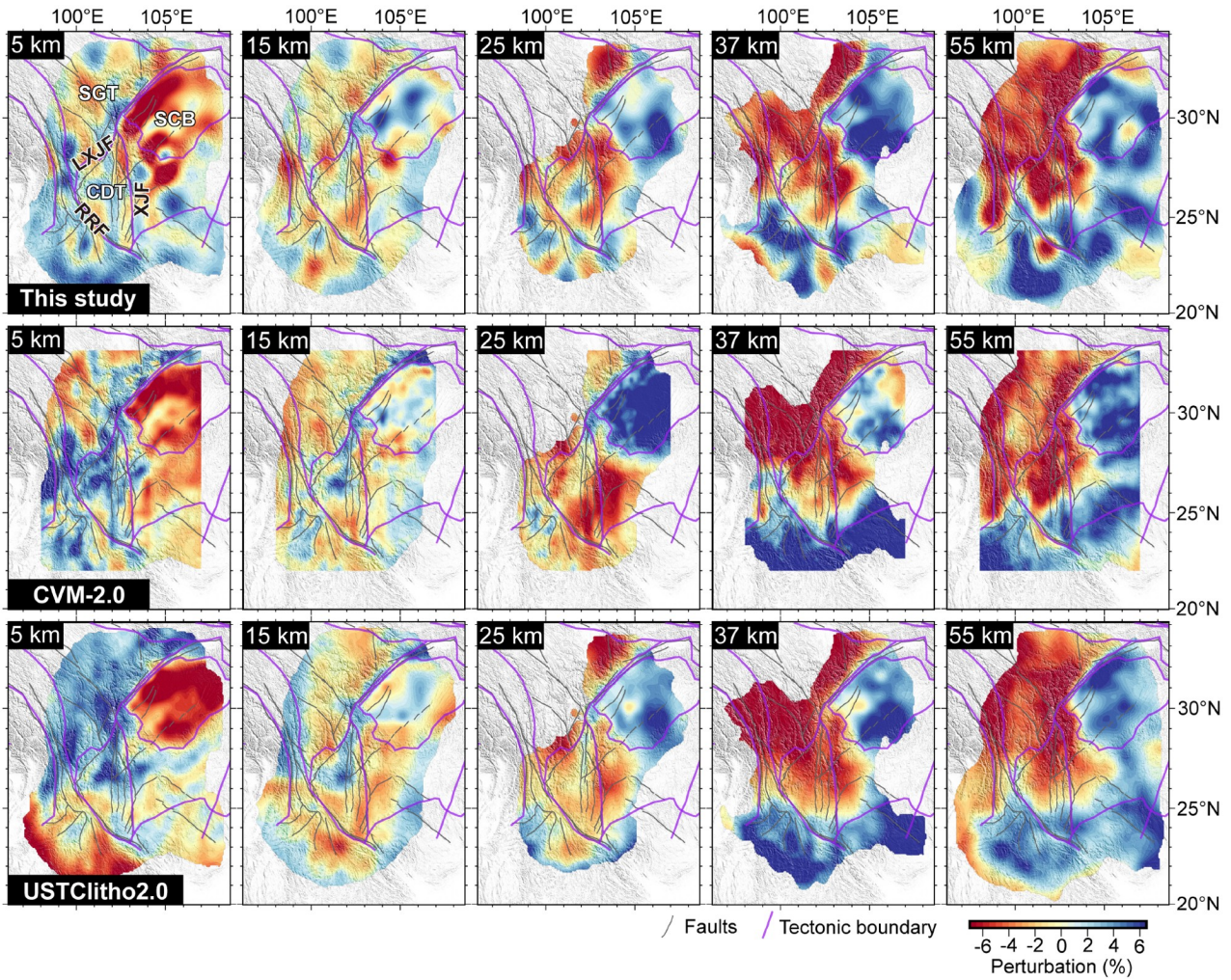


**Figure 8** Map views at five depths of the resulted isotropic  $V_p$  perturbation model, CVM2.0 and USTClitho2.0. The perturbation is relative to the average velocity at the given depth. We present the model only in the regions where  $R_{vel}(x) > 0.7$  at the given depth (as indicated by the dashed lines in Figure 4). The absolute P-wave velocity models are shown in Figure S9. The abbreviations of the tectonic blocks and faults are the same as in Figure 1.

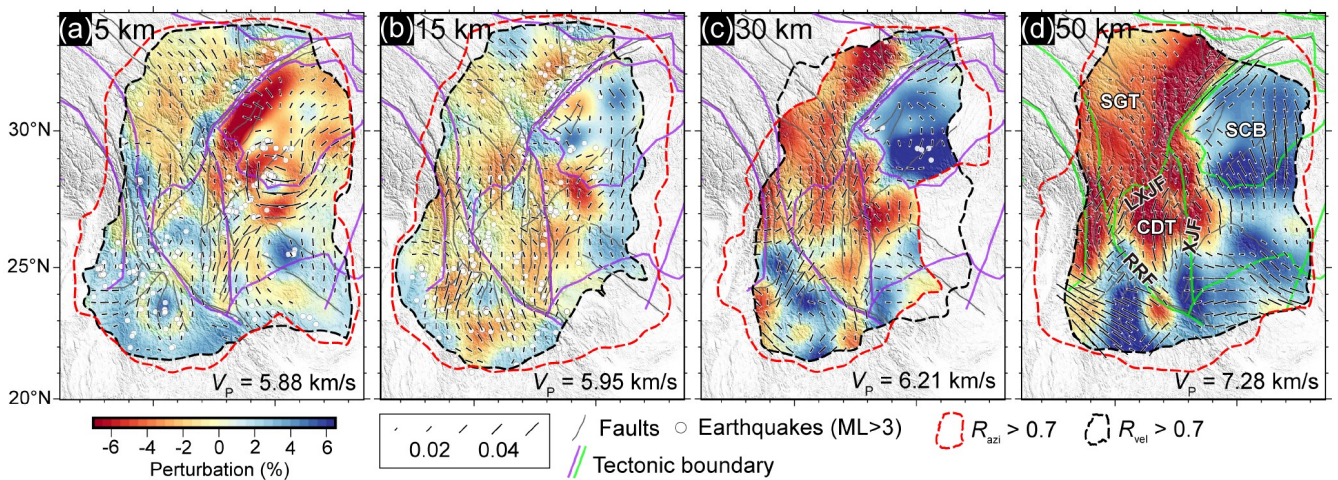


**Figure 9** Map views at four depths of 3D P-wave velocity and azimuthal anisotropy model. (a)–(d) Show the P-wave velocity perturbation model and the azimuthal anisotropy at different depths with the relocated earthquakes (white dots). The azimuthal anisotropy is represented by black bars. The perturbation is relative to the average velocity (labeled in the map) at the given depth. We present the model only in the intersection regions where the  $R_{vel}$  and  $R_{azi}$  are both greater than 0.7 (as indicated by the dashed lines in Figures 5 and 6). The abbreviations of the tectonic blocks and faults are the same as in Figure 1.

USTClitho2.0 integrate body wave arrival and surface wave dispersion data in a joint inversion. In addition, our model is updated using sensitivity kernels based on the traveltimes eikonal equation, whereas CVM2.0 and USTClitho2.0 use ray-tracing methods for model updating. Such data and methodological differences are likely to contribute to the observed discrepancies. Other factors, including inversion parameter settings and initial model selection, may also influence the model results (Zhang and Song, 2024). Furthermore, our checkerboard test results suggest a reasonable resolution in this region (Figure 4c). Further work is needed to investigate these model differences in more detail.

Recently, several 3D azimuthal anisotropy models have been developed for this region using Rayleigh waves (e.g., Han et al., 2022; Zhang Z et al., 2023). Overall, the azimuthal anisotropy structures are relatively similar, suggesting that both P-waves and surface waves provide consistent insights into the anisotropic properties of the medium. In the shallow crust (5 and 15 km depths), the azimuthal anisotropy directions in our model are generally consistent with those in Han et al. (2022) and Zhang Z et al. (2023), and are mainly aligned with the fault strike. At 30 km depth, these models all show a clockwise rotation in the anisotropy direction. Our model agrees with Han et al. (2022) and Zhang Z et al. (2023) in showing north-south and northeast-southwest anisotropy directions beneath the eastern Tibetan Plateau and the LXJF. However, there are differences in the XJF: Zhang Z et al. (2023) show a weak anisotropy with a north-south trend, and Han et al. (2022) show a north-south anisotropy, while our model shows a northwest-southeast anisotropy, almost perpendicular to the anisotropy direction beneath the LXJF. This anisotropy direction agrees well with the stress field direction obtained by Luo et al. (2016) from focal mechanism solutions, suggesting that the P-wave anisotropy structure may be more sensitive to the regional stress field. At lithospheric mantle depths, our model is generally consistent with Zhang Z et al. (2023), showing a prominent east-west anisotropy in the southern part of the CDT and a northwest-southeast anisotropy west of the RRF.

We also compare the anisotropy model in this study with other 3D P-wave azimuthal anisotropy models from previous studies. Recently, Huang et al. (2018) and Liu et al. (2022) develop P-wave azimuthal anisotropy models for the CDT and its adjacent region. Huang et al. (2018) use data from ChinArray from 2011 to 2012, and employ the 3D ray tracing method (Um and Thurber, 1987; Zhao et al., 1992) for ray tracing to obtain a P-wave azimuthal anisotropy model in the region. Liu et al. (2022) obtained the azimuthal anisotropy model using ray tracing based on traveltimes eikonal equation (Liu and Tong, 2021) with data from ChinArray and the China National Seismic Network (Zheng et al., 2010). For the sake of comparison, we generate slices at the same depths as Huang et al. (2018) (Figure S12).

In general, the north-south orientation of the FVDs in our model is consistent and agrees well with surface GPS measurements. However, there are notable differences in detail. In the depth range of 5–15 km (Figures 9 and S12), the FVDs in our model align well with the strike of faults, which is consistent with the results of Huang et al. (2018) and Liu et al. (2022). In addition, our model indicates minimal azimuthal anisotropy in the central part of the CDT, a feature less prominent in the models of Huang et al. (2018) and Liu et al. (2022). At depths around 30 to 50 km (Figure 9), there are some differences in the distribution of low-velocity anomalies between the models. In our model, the clockwise rotation of the FVD is more consistent with surface GPS displacement measurements than in the Huang et al. (2018) and Liu et al. (2022) models. In addition, our model more clearly highlights differences in azimuthal anisotropy beneath the LXJF and the XJF, suggesting different tectonic settings and material properties in these areas. At a depth of 50 km, the east-west FVD in the southern part of our study area is also more consistent with shear-wave splitting measurements. Unlike the comparisons between isotropic models (Figure 8), the differences between azimuthal anisotropy models are more pronounced. This may be attributed to the complexity introduced by azimuthal anisotropy inversion parameters, resulting in the inversion process more complicated. Furthermore, variations in data and methodology also contribute to these differences.

## 6.2 Comparison of azimuthal anisotropy model with shear-wave splitting measurements

Many studies publish their shear-wave splitting (SWS) measurements in the southeastern Tibetan Plateau (Figure S13; e.g., Shi et al., 2012, 2013; Chang et al., 2015; Zhang and Gao, 2017). SWS from local earthquakes measures the polarization direction of fast shear-wave (referred to as FPDs) and generally indicates crustal anisotropy (Crampin and Gao, 2006; Li Y et al., 2021). At depths of 5 and 15 km, the FVDs in our model are generally consistent with the FPDs (Figure 9). These directions are also consistent with the strike of the faults, suggesting that the anisotropy is controlled by the fault structures. Tectonic XKS (SKS, SKKS, PKS) splitting, which primarily reflects the anisotropy in the upper mantle (Fouch and Rondenay, 2006), a prominent feature is the sudden change in the FPDs from north-south to east-west at about 26°N (Figure S13b; Sol et al., 2007). In our model, the characteristic of this change in anisotropy direction is particularly pronounced. At a depth of 50 km (Figure 9d), the FVDs in the ICB and YZC show high agreement with the FPDs from the XKS splitting. Previous studies of the Moho depth in these regions suggest a crustal thickness of about 30–40 km (Dong et al., 2020; Cheng et al., 2022). Therefore, the results of this study reflect azimuthal

anisotropy in the upper mantle, which may indicate the direction of mantle flow. However, this east-west FVD is less pronounced in the results of [Huang et al. \(2018\)](#) and [Liu et al. \(2022\)](#), which may be due to limitations in methods and data resolution.

### 6.3 The relationship between seismic activity, velocity structure and fault zones

In this study, we also performed earthquake relocation during the inversion process, accounting for the effects of anisotropic structures (Figure S10). The horizontal and vertical profiles (Figures 9 and 10) show that seismic activity is mainly concentrated in the transition zones between high- and low-velocity anomalies. In profiles A and B (Figure 10), earthquakes beneath the XJF are mainly distributed along the outer edge of the low-velocity zone, especially in profile A. Near the LMSF, profile D clearly shows two fault-driven earthquake clusters, both located in areas with significant velocity contrasts. These observations are consistent with findings from several studies (e.g., [Wei et al., 2010](#); [Wang and Gao, 2014](#); [Dong et al., 2023](#); [Liu et al., 2023](#)), which suggest that low-velocity zones are less prone to rupture due to the ductile nature of the rock. In contrast, high-velocity anomalies are likely to indicate brittle rock properties, making the transition zones between high- and low-velocity anomalies more susceptible to deformation and rupture under fault stress and southeastern compression from the Tibetan Plateau, resulting in seismic activity.

The relocated earthquake locations show a strong correlation between seismic events and fault zones. Compared to the original earthquake locations, the relocated distribution is more concentrated. This study provides a profile analysis of seismic activity along major fault zones (Figure 11), showing varying levels of seismic activity at different locations along the same fault zone. Seismic activity beneath the LMSF is particularly intense, with several earthquakes exceeding magnitude 6, including the  $M_s$  8.0 Wenchuan earthquake in 2008 and the  $M_s$  7.0 Lushan earthquake in 2013. In profile EE' (Figure 11), seismicity is particularly concentrated in the northern segment of the LMSF, with earthquake depths predominantly between 10 and 20 km. A notable seismic gap is observed around 103°E. The uneven spatial distribution of seismic activity suggests an ongoing risk of large earthquakes in this region (e.g., [Liang et al., 2018](#); [Zheng and Guo, 2021](#)). The RRF also shows a clear segmentation (profile FF'). In the northern segment of the Red River Fault, seismicity is more frequent, probably due to the intersection with the LXJF, which creates a complex stress field and increases earthquake activity. In contrast, the southern segment of the RRF has significantly lower seismicity, even where it intersects with the XJF ([Wang F et al., 2014](#); [Wan et al., 2021](#)). Based on extensive geophysical and geological

data, [Li and Gao \(2024\)](#) concluded that the RRF shows strong segmentation, a view supported by our velocity and anisotropy results. At crustal depths in the northern segment of the Red River Fault, our model shows the FVDs nearly parallel to the fault strike, appearing as north-south or northeast-southwest (Figure 9). In contrast, the southern segment shows either weak anisotropy or north-south anisotropy, forming a certain angle with the fault strike. In terms of P-wave velocity, the northern segment shows generally similar velocity anomalies on both sides, while the southern segment shows stronger velocity contrasts, particularly at 30 km depth (Figure 9c). This suggests that the southern segment of the Red River Fault plays a greater role in controlling material movement and stress distribution in the region ([Li and Gao, 2024](#)), while the northern segment may have a lesser influence. At 50 km depth, the FVDs of the southern segment show an east-west orientation, while the northern segment remains north-south, suggesting that the anisotropy shift in the southern segment indicates that the RRF does not extend into the lithospheric mantle. Profile GG' shows relatively high seismic activity at the intersections of the XSHF and DLSF, as well as the DLSF and XJF, while the central parts of these fault zones show lower seismic activity. The HH' profile also shows stronger seismic activity on the northern side of the ANF compared to the southern side. These observations suggest that complex fault systems at fault intersections may be more sensitive to stress loading ([Andrews, 1989](#); [Ben-Zion and Sammis, 2003](#); [Lee et al., 2024](#)).

## 7. Conclusions

This study utilizes P-wave first-arrival data selected from the earthquake catalogs provided by the China Earthquake Administration, covering the period from 2008 to 2022. From these data, we construct both common-receiver and common-source differential traveltimes datasets. Applying a newly developed adjoint traveltimes tomography method, we jointly invert the absolute and differential traveltimes data to obtain a 3D P-wave velocity and azimuthal anisotropy model beneath the southeastern margin of the Tibetan Plateau. Checkerboard resolution tests indicate that the model is reliable over most of the study area. In addition, the results agree well with previous tomographic studies and shear wave splitting measurements, revealing further structural details.

Our results show that at shallow crustal depths, the central region of the CDT and the core of the ELIP exhibit relatively weak azimuthal anisotropy. At 30 km depth, significant low-velocity anomalies are observed beneath the SGT, LXJF and XJF. However, there are distinct differences in the anisotropic patterns of these anomalies: beneath the SGT and

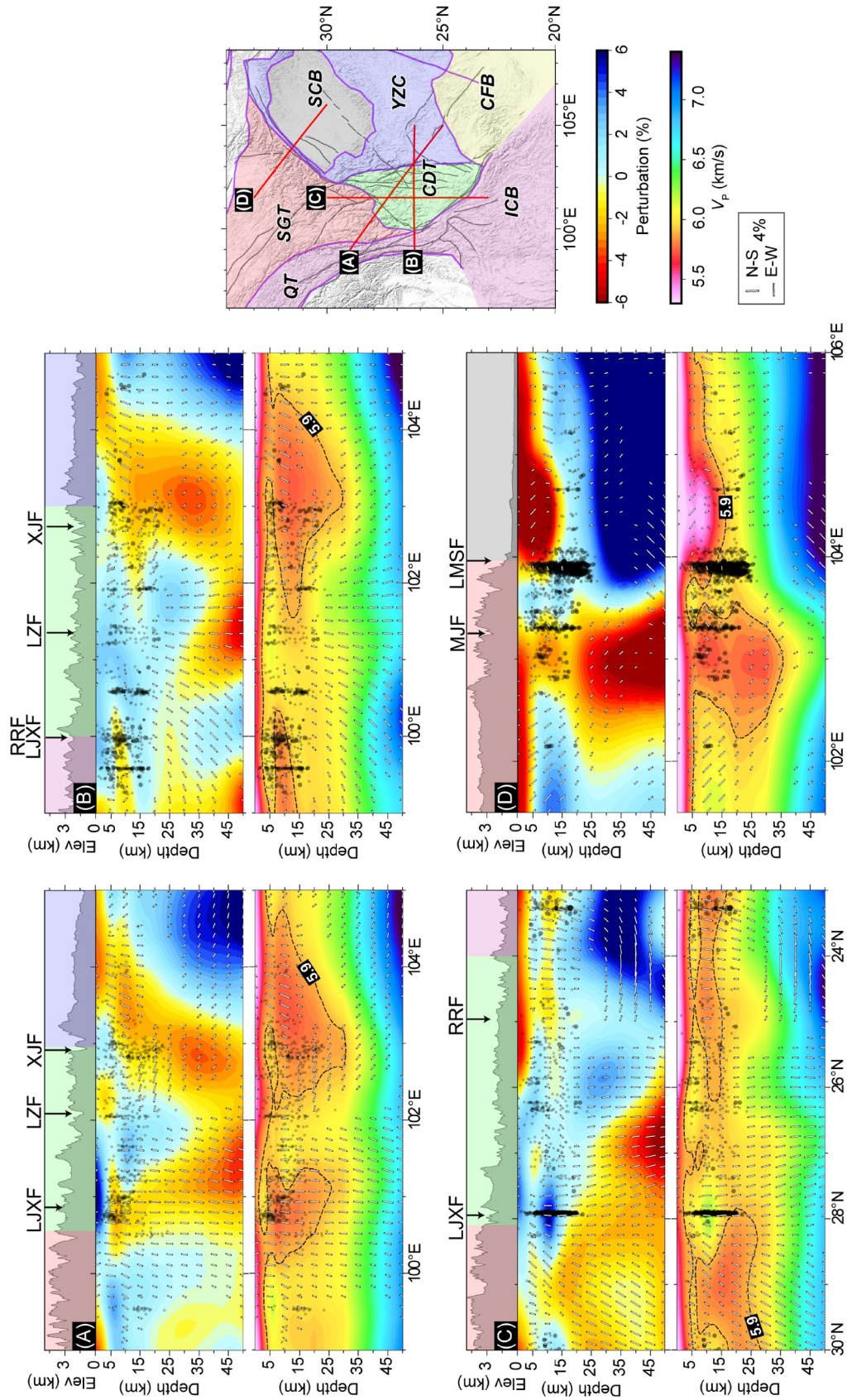


**Figure 10** Four vertical profiles of anisotropic P-wave velocity and azimuthal anisotropy models. The locations of the profiles are shown on the small map on the right. For each vertical profile, velocity perturbations and absolute velocity are shown, with black dots representing relocated earthquakes. The velocity perturbations are relative to the average velocity for that profile. White bars represent the azimuthal anisotropy results. The terrain color corresponds to the block colors in the small map on the right. The abbreviations for tectonic blocks and faults are the same as in Figure 1.

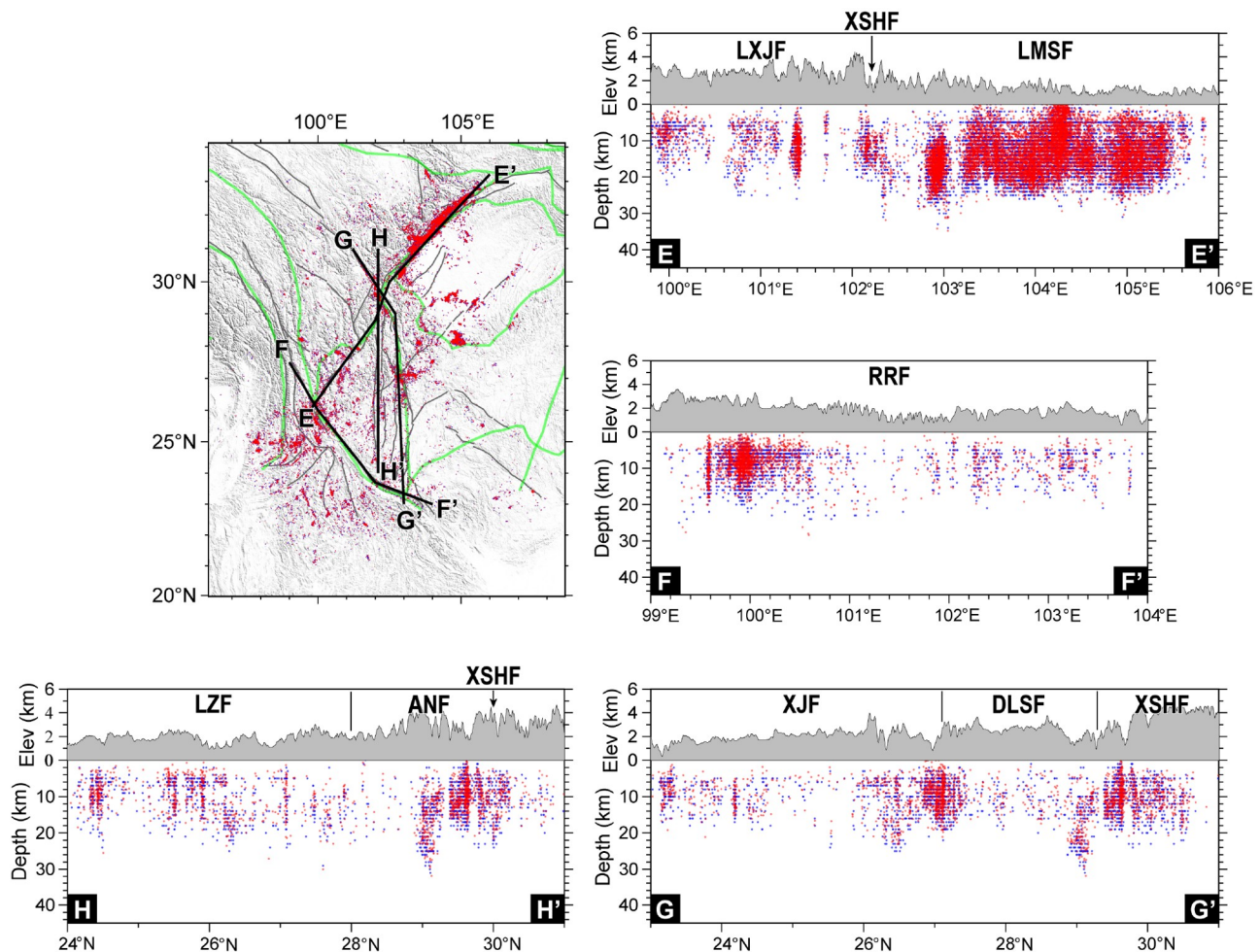


**Figure 11** Earthquake distribution before and after relocation along major fault zones. This figure shows four vertical profiles along major fault zones, with blue and red dots representing the earthquakes before and after relocation. The profiles show earthquakes within 30 km of the profile line. The grey shading represents the topography of the profile. The abbreviations for the major faults are the same as in Figure 1.

LXJF, the FVD aligns north-south or northeast-southwest, whereas beneath the XJF it aligns northwest-southeast. This contrast suggests significant differences in material properties and tectonic setting between these regions. In the southern part of the study area, in contrast to other tomographic models, our results highlight a pronounced east-west anisotropy at upper mantle depths, which agrees well with teleseismic shear wave splitting observations. In terms of seismic activity, high levels of seismicity are observed in regions of sharp velocity contrasts across the southeastern margin of the Tibetan Plateau and are closely associated with major fault zones. Both the RRF and XJF show spatially heterogeneous seismic activity, and a significant seismic gap is observed in the southern segment of the LMSF. Earthquakes also occur more frequently at fault intersections, such as where the northern RRF intersects the LXJF and along the northern segment of the XJF. The newly derived P-wave velocity and anisotropy model from this study provides new insights into tectonic deformation and seismogenic mechanisms beneath the southeastern Tibetan Plateau.

**Acknowledgements** The authors thank the anonymous reviewers and scientific editor for their constructive and insightful comments, which helped improved the manuscript. The authors also thank Dr. Shuyu LI for providing the shear-wave splitting data. The traveltimes dataset is provided by China Earthquake data Center (<http://data.earthquake.cn/>). The figures were generated by GMT (<https://www.generic-mapping-tools.org/>) and Matplotlib (<https://matplotlib.org/>). This study was supported by the National Key R&D Program of China (Grant No. 2022YFF0800601) and the China National Science and Technology Major Project (Grant 2024ZD1001101).

**Conflict of interest** The authors declare that they have no conflict of interest.

## References

- Ali J R, Thompson G M, Zhou M F, Song X. 2005. Emeishan large igneous province, SW China. *Lithos*, 79: 475–489
- Allam A A, Ben-Zion Y. 2012. Seismic velocity structures in the southern California plate-boundary environment from double-difference tomography. *Geophys J Int*, 190: 1181–1196
- Andrews D J. 1989. Mechanics of fault junctions. *J Geophys Res*, 94: 9389–9397
- Bai D, Unsworth M J, Meju M A, Ma X, Teng J, Kong X, Sun Y, Sun J,

- Wang L, Jiang C, Zhao C, Xiao P, Liu M. 2010. Crustal deformation of the eastern Tibetan plateau revealed by magnetotelluric imaging. *Nat Geosci*, 3: 358–362
- Bao X, Sun X, Xu M, Eaton D W, Song X, Wang L, Ding Z, Mi N, Li H, Yu D, Huang Z, Wang P. 2015. Two crustal low-velocity channels beneath SE Tibet revealed by joint inversion of Rayleigh wave dispersion and receiver functions. *Earth Planet Sci Lett*, 415: 16–24
- Bao X, Song X, Eaton D W, Xu Y, Chen H. 2020. Episodic lithospheric deformation in eastern Tibet inferred from seismic anisotropy. *Geophys Res Lett*, 47: e2019GL085721
- Beaumont C, Jamieson R A, Nguyen M H, Lee B. 2001. Himalayan tectonics explained by extrusion of a low-viscosity crustal channel coupled to focused surface denudation. *Nature*, 414: 738–742
- Ben-Zion Y, Sammis C G. 2003. Characterization of fault zones. *Pure Appl Geophys*, 160: 677–715
- Boness N L, Zoback M D. 2006. Mapping stress and structurally controlled crustal shear velocity anisotropy in California. *Geology*, 34: 825
- Boyd O S, Jones C H, Sheehan A F. 2004. Foundering lithosphere imaged beneath the southern Sierra Nevada, California, USA. *Science*, 305: 660–662
- Burchfiel B C, Chen Z. 2013. Tectonics of the Southeastern Tibetan Plateau and its Adjacent Foreland. Boulder: Geological Society of America
- Cao F, Liang C, Zhou L, Zhu J. 2020. Seismic azimuthal anisotropy for the southeastern Tibetan Plateau extracted by wave gradiometry analysis. *J Geophys Res-Solid Earth*, 125: e2019JB018395
- Chang L, Ding Z, Wang C. 2015. Upper mantle anisotropy beneath the southern segment of North-South tectonic belt, China (in Chinese). *Chin J Geophys*, 58: 4052–4067
- Chen G, Chen J, Tape C, Wu H, Tong P. 2023. Double-difference adjoint tomography of the crust and uppermost mantle beneath Alaska. *J Geophys Res-Solid Earth*, 128: e2022JB025168
- Chen J, Chen G, Nagaso M, Tong P. 2023a. Adjoint-state traveltimes tomography for azimuthally anisotropic media in spherical coordinates. *Geophys J Int*, 234: 712–736
- Chen J, Wu S, Xu M, Nagaso M, Yao J, Wang K, Li T, Bai Y, Tong P. 2023b. Adjoint-state teleseismic traveltimes tomography: Method and application to Thailand in Indochina Peninsula. *J Geophys Res-Solid Earth*, 128: e2023JB027348
- Chen M, Niu F, Liu Q, Tromp J, Zheng X. 2015. Multiparameter adjoint tomography of the crust and upper mantle beneath East Asia: 1. Model construction and comparisons. *J Geophys Res-Solid Earth*, 120: 1762–1786
- Cheng S, Xiao X, Wu J, Wang W, Sun L, Wang X, Wen L. 2022. Crustal thickness and  $V_p/V_s$  variation beneath continental China revealed by receiver function analysis. *Geophys J Int*, 228: 1731–1749
- Clark M K, Royden L H. 2000. Topographic ooze: Building the eastern margin of Tibet by lower crustal flow. *Geology*, 28: 703
- Copley A, McKenzie D. 2007. Models of crustal flow in the India-Asia collision zone. *Geophys J Int*, 169: 683–698
- Crampin S, Gao Y. 2006. A review of techniques for measuring shear-wave splitting above small earthquakes. *Phys Earth Planet Inter*, 159: 1–14
- Crampin S, Chesnokov E M, Hipkin R G. 1984. Seismic anisotropy—The state of the art: II. *Geophys J Int*, 76: 1–16
- Deng Q, Zhang P, Ran Y, Yang X, Min W, Chu Q. 2003. Basic characteristics of active tectonics of China. *Sci China Ser D-Earth Sci*, 46: 356–372
- Ding L, Kapp P, Cai F, Garzzone C N, Xiong Z, Wang H, Wang C. 2022. Timing and mechanisms of Tibetan Plateau uplift. *Nat Rev Earth Environ*, 3: 652–667
- Dong L, Shen X, Qian Y. 2020. Study on velocity and density contrasts across the Moho in the southeastern margin of the Tibetan Plateau (in Chinese). *Chin J Geophys*, 63: 915–927
- Dong X, Yang D. 2022. Positions of large earthquakes revealed from velocity heterogeneities and radial anisotropy in the eastern Tibetan Plateau. *Sci Bull*, 67: 2026–2029
- Dong X, Yang D, Niu F. 2019. Passive adjoint tomography of the crustal and upper mantle beneath eastern Tibet with a W2-norm misfit function. *Geophys Res Lett*, 46: 12986–12995
- Dong X, Yang D, Meng W. 2023. Melt/fluid migration and the 2022 Luding  $M_s$  6.8 earthquake. *Chin Sci Bull*, 68: 2642–2647
- Du G, Wu Q, Zhang X, He J, Zou L, Feng Y, Liu J, Romanelli F. 2019. Pn wave velocity and anisotropy underneath the central segment of the North-South Seismic Belt in China. *J Asian Earth Sci*, 184: 103941
- England P, Houseman G. 1986. Finite strain calculations of continental deformation: 2. Comparison with the India-Asia Collision Zone. *J Geophys Res*, 91: 3664–3676
- England P C, Houseman G A. 1988. The mechanics of the Tibetan Plateau. *Phil Trans R Soc Lond A*, 326: 301–320
- Feng M, An M, Mechie J, Zhao W, Xue G, Su H. 2020. Lithospheric structures of and tectonic implications for the central-east Tibetan plateau inferred from joint tomography of receiver functions and surface waves. *Geophys J Int*, 223: 1688–1707
- Fouch M J, Rondenay S. 2006. Seismic anisotropy beneath stable continental interiors. *Phys Earth Planet Inter*, 158: 292–320
- Gao Y, Shi Y, Wang Q. 2020. Seismic anisotropy in the southeastern margin of the Tibetan Plateau and its deep tectonic significances (in Chinese). *Chin J Geophys*, 63: 802–816
- Han C, Xu M, Huang Z, Wang L, Xu M, Mi N, Yu D, Gou T, Wang H, Hao S, Tian M, Bi Y. 2020. Layered crustal anisotropy and deformation in the SE Tibetan Plateau revealed by Markov-Chain-Monte-Carlo inversion of receiver functions. *Phys Earth Planet Inter*, 306: 106522
- Han C, Huang Z, Hao S, Wang L, Xu M, Hammond J O S. 2022. Restricted lithospheric extrusion in the SE Tibetan Plateau: Evidence from anisotropic Rayleigh-wave tomography. *Earth Planet Sci Lett*, 598: 117837
- Han S, Zhang H, Xin H, Shen W, Yao H. 2021. USTClitho2.0: Updated unified seismic tomography models for continental china lithosphere from joint inversion of body-wave arrival times and surface-wave dispersion data. *Seismol Res Lett*, 93: 201–215
- Hou Z, Liu L, Zhang H, Xu B, Wang Q, Yang T, Wang R, Zheng Y, Li Y, Gao L, Yu N, Wang X, Miao Z, Han S, Lü Q. 2024. Cenozoic eastward growth of the Tibetan Plateau controlled by tearing of the Indian slab. *Nat Geosci*, 17: 255–263
- Hu J, Badal J, Yang H, Li G, Peng H. 2018. Comprehensive crustal structure and seismological evidence for lower crustal flow in the southeastern margin of Tibet revealed by receiver functions. *Gondwana Res*, 55: 42–59
- Hu L, Zhang F, Li Y. 2024. Crustal velocity structure of the Sichuan-Yunnan block revealed by high-quality crustal phase travel time. *Seismol Res Lett*, 95: 1913–1925
- Hua Y, Zhang S, Li M, Wu T, Qin W, Wang F, Zhang B. 2018. A new geodynamic model related to seismicity beneath the southeastern margin of the Tibetan Plateau revealed by regional tomography. *Geophys J Int*, 214: 933–951
- Huang F, Bao X, Dai Q A, Li X. 2024. Structural similarity of lithospheric velocity models of Chinese mainland. *Earthquake Sci*, 37: 514–528
- Huang J, Song X, Wang S. 2003. Fine structure of Pn velocity beneath Sichuan-Yunnan region. *Sci China Ser D-Earth Sci*, 46: 201–209
- Huang J, Liu X, Su Y, Wang B. 2012. Imaging 3-D crustal P-wave velocity structure of western Yunnan with bulletin data. *Earthquake Sci*, 25: 151–160
- Huang Z, Chevrot S. 2021. Mantle dynamics in the SE Tibetan Plateau revealed by teleseismic shear-wave splitting analysis. *Phys Earth Planet Inter*, 313: 106687
- Huang Z, Wang P, Xu M, Wang L, Ding Z, Wu Y, Xu M, Mi N, Yu D, Li H. 2015. Mantle structure and dynamics beneath SE Tibet revealed by new seismic images. *Earth Planet Sci Lett*, 411: 100–111
- Huang Z, Wang L, Xu M, Zhao D. 2018. P wave anisotropic tomography of the SE Tibetan Plateau: Evidence for the crustal and upper-mantle deformations. *J Geophys Res-Solid Earth*, 123: 8957–8978
- Huang Z, Ji C, Wu H, Shi Y, Geng J, Xu M, Han C, Xu M, Wang L. 2021. Review on the crustal structures and deformations in the southeastern margin of the Tibetan Plateau (in Chinese). *Rev Geophys Planet Phys*, 52: 291–307
- Kind R, Yuan X, Saul J, Nelson D, Sobolev S V, Mechie J, Zhao W, Kosarev G, Ni J, Achauer U, Jiang M. 2002. Seismic images of crust and upper mantle beneath Tibet: Evidence for Eurasian Plate subduction. *Science*, 298: 1219–1221

- Kong F, Wu J, Liu L, Liu K H, Song J, Li J, Gao S S. 2018. Azimuthal anisotropy and mantle flow underneath the southeastern Tibetan Plateau and northern Indochina Peninsula revealed by shear wave splitting analyses. *Tectonophysics*, 747-748: 68–78
- Lee J, Tsai V C, Hirth G, Chatterjee A, Trugman D T. 2024. Fault-network geometry influences earthquake frictional behaviour. *Nature*, 631: 106–110
- Lei J, Li Y, Xie F, Teng J, Zhang G, Sun C, Zha X. 2014. Pn anisotropic tomography and dynamics under eastern Tibetan plateau. *J Geophys Res-Solid Earth*, 119: 2174–2198
- Lévéque J J, Rivera L, Wittlinger G. 1993. On the use of the checker-board test to assess the resolution of tomographic inversions. *Geophys J Int*, 115: 313–318
- Li L, Zhang X, Liao J, Liang Y, Dong S. 2021. Geophysical constraints on the nature of lithosphere in central and eastern Tibetan Plateau. *Tectonophysics*, 804: 228722
- Li X, Ma X, Chen Y, Xue S, Varentsov I M, Bai D. 2020. A plume-modified lithospheric barrier to the southeastward flow of partially molten Tibetan crust inferred from magnetotelluric data. *Earth Planet Sci Lett*, 548: 116493
- Li Y, Gao Y. 2024. Segmental nature of the Red River fault revealed by seismic anisotropy and geological structures. *Sci China Earth Sci*, 67: 2423–2443
- Li Y, Gao Y, Shi Y, Wu P. 2021. Preliminary seismic anisotropy in the upper crust of the south segment of Xiaojiang faults and its tectonic implications. *Earthquake Sci*, 34: 64–76
- Liang C, Song X, Huang J. 2004. Tomographic inversion of Pn travel times in China. *J Geophys Res*, 109: 2003JB002789
- Liang C, Song X. 2006. A low velocity belt beneath northern and eastern Tibetan Plateau from Pn tomography. *Geophys Res Lett*, 33: L22306
- Liang C, Huang Y, Wang C, Liu Z, Yang Y, Wu J, He F. 2018. Progress in the studies of the seismic gap between the 2008 Wenchuan and 2013 Lushan earthquakes (in Chinese). *Chin J Geophys*, 61: 1996–2010
- Liang C, Liu Z, Hua Q, Wang L, Jiang N, Wu J. 2020. The 3D seismic azimuthal anisotropies and velocities in the eastern Tibetan Plateau extracted by an azimuth-dependent dispersion curve inversion method. *Tectonics*, 39: e2019TC005747
- Liu C, Yao H, Yang H Y, Shen W, Fang H, Hu S, Qiao L. 2019. Direct inversion for three-dimensional shear wave speed azimuthal anisotropy based on surface wave ray tracing: Methodology and application to Yunnan, southwest China. *J Geophys Res-Solid Earth*, 124: 11394–11413
- Liu Q Y, van der Hilst R D, Li Y, Yao H J, Chen J H, Guo B, Qi S H, Wang J, Huang H, Li S C. 2014. Eastward expansion of the Tibetan Plateau by crustal flow and strain partitioning across faults. *Nat Geosci*, 7: 361–365
- Liu S, Yang Y, Deng B, Zhong Y, Wen L, Sun W, Li Z, Jansa L, Li J, Song J, Zhang X, Peng H. 2021. Tectonic evolution of the Sichuan Basin, southwest China. *Earth-Sci Rev*, 213: 103470
- Liu S, Chang K, Yang D, Xu X, Wang W, Yang S, Li M. 2022. Velocity and azimuthal anisotropy structures beneath the Dianzhong Block and its vicinity, SE Tibetan Plateau, revealed by eikonal equation-based traveltimes tomography. *Tectonophysics*, 839: 229525
- Liu Y, Tong P. 2021. Eikonal equation-based P-wave seismic azimuthal anisotropy tomography of the crustal structure beneath northern California. *Geophys J Int*, 226: 287–301
- Liu Y, Yao H, Zhang H, Fang H. 2021. The community velocity model V.1.0 of southwest China, constructed from joint body- and surface-wave travel-time tomography. *Seismol Res Lett*, 92: 2972–2987
- Liu Y, Yu Z, Zhang Z, Yao H, Wang W, Zhang H, Fang H, Fang L. 2023. The high-resolution community velocity model V2.0 of southwest China, constructed by joint body and surface wave tomography of data recorded at temporary dense arrays. *Sci China Earth Sci*, 66: 2368–2385
- Lü Y, Ni S, Liu B, Sun Y. 2011. P n tomographic velocity and anisotropy beneath the Tibetan Plateau and the adjacent regions. *Earth Planet Sp*, 63: 1169–1173
- Luo S, Qian J. 2012. Fast sweeping methods for factored anisotropic Eikonal equations: Multiplicative and additive factors. *J Sci Comput*, 52: 360–382
- Luo J, Zhao C, Lü J, Zhou L, Zheng S. 2016. Characteristics of focal mechanisms and the stress field in the southeastern margin of the Tibetan Plateau. *Pure Appl Geophys*, 173: 2687–2710
- Molnar P, Tapponnier P. 1975. Cenozoic Tectonics of Asia: Effects of a Continental Collision: Features of recent continental tectonics in Asia can be interpreted as results of the India-Eurasia collision. *Science*, 189: 419–426
- Montagner J P, Guillot L. 2002. Seismic anisotropy and global geodynamics. *Rev Mineral Geochem*, 51: 353–385
- Nie S, Tian X, Li J, Tan P. 2021. Lithospheric mantle underneath the Tibetan Plateau does not escape southeastward. *J Asian Earth Sci*, 206: 104629
- Peng H, Gao Z, Hu J, Yang H, Badal J, Chen M, Zhang T. 2022. Upper mantle anisotropy in the southeastern margin of the Tibetan plateau and geodynamic implications. *Phys Earth Planet Inter*, 327: 106877
- Peltzer G, Tapponnier P. 1988. Formation and evolution of strike-slip faults, rifts, and basins during the India-Asia Collision: An experimental approach. *J Geophys Res*, 93: 15085–15117
- Qiao L, Yao H, Lai Y C, Huang B S, Zhang P. 2018. Crustal structure of southwest China and northern Vietnam from ambient noise tomography: Implication for the large-scale material transport model in SE Tibet. *Tectonics*, 37: 1492–1506
- Rawlinson N, Hauser J, Sambridge M. 2008. Seismic ray tracing and wavefront tracking in laterally heterogeneous media. *Adv Geophys*, 49: 203–273
- Rawlinson N, Spakman W. 2016. On the use of sensitivity tests in seismic tomography. *Geophys J Int*, 205: 1221–1243
- Royden L H, Burchfiel B C, King R W, Wang E, Chen Z, Shen F, Liu Y. 1997. Surface deformation and lower crustal flow in eastern Tibet. *Science*, 276: 788–790
- Royden L H, Burchfiel B C, van der Hilst R D. 2008. The geological evolution of the Tibetan Plateau. *Science*, 321: 1054–1058
- Rui X, Stamps D S. 2019. A geodetic strain rate and tectonic velocity model for China. *Geochem Geophys Geosyst*, 20: 1280–1297
- Schoenbohm L M, Burchfiel B C, Chen L Z. 2006. Propagation of surface uplift, lower crustal flow, and Cenozoic tectonics of the southeast margin of the Tibetan Plateau. *Geology*, 34: 813–816
- Shellnutt J G. 2014. The Emeishan large igneous province: A synthesis. *Geosci Front*, 5: 369–394
- Shen Z K, Lü J, Wang M, Bürgmann R. 2005. Contemporary crustal deformation around the southeast borderland of the Tibetan Plateau. *J Geophys Res*, 110: 2004JB003421
- Shi Y, Gao Y, Su Y, Wang Q. 2012. Shear-wave splitting beneath Yunnan area of Southwest China. *Earthq Sci*, 25: 25–34
- Shi Y, Gao Y, Zhang Y, Wang H, Yao Z. 2013. Shear-wave splitting in the crust in Eastern Songpan-Garzê block, Sichuan-Yunnan block and Western Sichuan Basin (in Chinese). *Chin J Geophys*, 56: 481–494
- Sol S, Meltzer A, Bürgmann R, van der Hilst R D, King R, Chen Z, Koons P O, Lev E, Liu Y P, Zeitler P K, Zhang X, Zhang J, Zurek B. 2007. Geodynamics of the southeastern Tibetan Plateau from seismic anisotropy and geodesy. *Geology*, 35: 563–566
- Tapponnier P, Peltzer G, Le Dain A Y, Armijo R, Cobbold P. 1982. Propagating extrusion tectonics in Asia: New insights from simple experiments with plasticine. *Geology*, 10: 611–616
- Tapponnier P, Zhiqin X, Roger F, Meyer B, Arnaud N, Wittlinger G, Jingsui Y. 2001. Oblique stepwise rise and growth of the Tibet Plateau. *Science*, 294: 1671–1677
- Tong P. 2021a. Adjoint-state traveltimes tomography: Eikonal equation-based methods and application to the Anza area in southern California. *J Geophys Res-Solid Earth*, 126: e2021JB021818
- Tong P. 2021b. Adjoint-state traveltimes tomography for azimuthally anisotropic media and insight into the crustal structure of central California near Parkfield. *J Geophys Res-Solid Earth*, 126: e2021JB022365
- Tong P, Yang D, Huang X. 2019. Multiple-grid model parametrization for seismic tomography with application to the San Jacinto fault zone. *Geophys J Int*, 218: 200–223
- Tong P, Li T, Chen J, Nagaso M. 2023. Adjoint-state differential arrival

- time tomography. *Geophys J Int*, 236: 139–160
- Um J, Thurber C. 1987. A fast algorithm for two-point seismic ray tracing. *Bull Seismol Soc Am*, 77: 972–986
- Waldhauser F, Ellsworth W L. 2000. A double-difference earthquake location algorithm: Method and application to the northern Hayward Fault, California. *Bull Seismol Soc Am*, 90: 1353–1368
- Wan Y, Shen X, Liu R, Liu X, Zheng Z, Li Y, Zhang Y, Wang L. 2021. Present slip and stress distribution of block boundary faults in the sichuan-yunnan region (in Chinese). *Seismol Geol*, 43: 1614–1637
- Wang C, Dai J, Zhao X, Li Y, Graham S A, He D, Ran B, Meng J. 2014. Outward-growth of the Tibetan Plateau during the Cenozoic: A review. *Tectonophysics*, 621: 1–43
- Wang F, Pan S, Liu L, Liu B, Zhang J, Deng X, Ma C, Zhang C. 2014. Wide angle seismic exploration of Yuxi-Lincang profile—The research of crustal structure of the red river fault zone and southern Yunnan (in Chinese). *Chin J Geophys*, 57: 3247–3258
- Wang M, Shen Z K. 2020. Present-day crustal deformation of continental China derived from GPS and its tectonic implications. *J Geophys Res-Solid Earth*, 125: e2019JB018774
- Wang Q, Gao Y. 2014. Rayleigh wave phase velocity tomography and strong earthquake activity on the southeastern front of the Tibetan Plateau. *Sci China Earth Sci*, 57: 2532–2542
- Wang S, Xu X, Hu J. 2015. Review on the study of crustal structure and geodynamic models for the southeast margin of the Tibetan Plateau (in Chinese). *Chin J Geophys*, 58: 4235–4253
- Wang X, Chen L, Yao H. 2021. A new body-wave amplitude ratio-based method for imaging shallow crustal structure and its application in the Sichuan Basin, southwestern China. *Geophys Res Lett*, 48: e2021GL095186
- Wei W, Sun R M, Shi Y L. 2010. P-wave tomographic images beneath southeastern Tibetan Plateau: Investigating the mechanism of the 2008 Wenchuan earthquake. *Sci China Earth Sci*, 53: 1252–1259
- Wei W, Zhao D, Xu J. 2013. P-wave anisotropic tomography in Southeast Tibet: New insight into the lower crustal flow and seismotectonics. *Phys Earth Planet Inter*, 222: 47–57
- Wei Z, Zhao L. 2022. P-wave velocity structure of the lower crust and uppermost mantle beneath the Sichuan-Yunnan (China) region. *Seismol Res Lett*, 93: 2161–2175
- Weiss T, Siegesmund S, Rabbel W, Bohlen T, Pohl M. 1999. Seismic velocities and anisotropy of the lower continental crust: A review. *Pure Appl Geophys*, 156: 97–122
- Wenk H R. 2002. Texture and anisotropy. *Rev Mineral Geochem*, 51: 291–329
- Wu J, Cai Y, Wang W, Wang W, Wang C, Fang L, Liu Y, Liu J. 2024. Three dimensional velocity model and its tectonic implications at China Seismic Experimental Site, eastern margin of the Tibetan Plateau. *Sci China Earth Sci*, 67: 2268–2290
- Wu Z, Li L. 2021. China seismic experimental site (CSES): A systems engineering perspective. *Earthquake Sci*, 34: 192–198
- Xia X, Li Z, Bao F, Xie J, Shi Y, You Q, Chen H. 2021. Sedimentary structure of the Sichuan Basin derived from seismic ambient noise tomography. *Geophys J Int*, 225: 54–67
- Xiao Z, Fuji N, Iidaka T, Gao Y, Sun X, Liu Q. 2020. Seismic structure beneath the Tibetan Plateau from iterative finite-frequency tomography based on ChinArray: New insights into the Indo-Asian collision. *J Geophys Res-Solid Earth*, 125: e2019JB018344
- Xin H, Zhang H, Kang M, He R, Gao L, Gao J. 2019. High-resolution lithospheric velocity structure of continental china by double-difference seismic travel-time tomography. *Seismol Res Lett*, 90: 229–241
- Xu Y G, He B, Chung S L, Menzies M A, Frey F A. 2004. Geologic, geochemical, and geophysical consequences of plume involvement in the Emeishan flood-basalt province. *Geology*, 32: 917
- Xu Y G, He B, Huang X, Luo Z, Chung S L, Xiao L, Zhu D, Shao H, Fan W M, Xu J, Wang Y J. 2007. Identification of mantle plumes in the Emeishan Large Igneous Province. *Episodes*, 30: 32–42
- Xu Z J, Song X. 2010. Joint inversion for crustal and Pn velocities and Moho depth in Eastern Margin of the Tibetan Plateau. *Tectonophysics*, 491: 185–193
- Yao H, van der Hilst R D, Beghein C. 2008. Surface wave array tomography in SE Tibet from ambient seismic noise and two-station analysis—II. Crustal and upper-mantle structure. *Geophys J Int*, 173: 205–219
- Yao H, van der Hilst R D, de Hoop M V. 2006. Surface-wave array tomography in SE Tibet from ambient seismic noise and two-station analysis—I. Phase velocity maps. *Geophys J Int*, 166: 732–744
- Yao H, van der Hilst R D, Montagner J P. 2010. Heterogeneity and anisotropy of the lithosphere of SE Tibet from surface wave array tomography. *J Geophys Res*, 115: 2009JB007142
- Yang Y, Ritzwoller M H, Zheng Y, Shen W, Levshin A L, Xie Z. 2012. A synoptic view of the distribution and connectivity of the mid-crustal low velocity zone beneath Tibet. *J Geophys Res*, 117: 2011JB008810
- Yin A, Harrison T M. 2000. Geologic evolution of the Himalayan-Tibetan orogen. *Annu Rev Earth Planet Sci*, 28: 211–280
- Yuan Y O, Simons F J, Tromp J. 2016. Double-difference adjoint seismic tomography. *Geophys J Int*, 206: 1599–1618
- Zelt C A. 1998. Lateral velocity resolution from three-dimensional seismic refraction data. *Geophys J Int*, 135: 1101–1112
- Zhang B, Zhang S, Wu T, Hua Y. 2018. Upper crustal anisotropy from local shear-wave splitting and crust-mantle coupling of Yunnan, SE margin of Tibetan Plateau. *Geodesy Geodyn*, 9: 302–311
- Zhang H, Thurber C. 2003. Double-difference tomography: The method and its application to the Hayward Fault, California. *Bull Seismol Soc Am*, 93: 1875–1889
- Zhang H, Thurber C. 2006. Development and applications of double-difference seismic tomography. *Pure Appl Geophys*, 163: 373–403
- Zhang P Z. 2013. A review on active tectonics and deep crustal processes of the Western Sichuan region, eastern margin of the Tibetan Plateau. *Tectonophysics*, 584: 7–22
- Zhang X, Song X. 2024. Assessing the effects of model parameter assumptions on surface-wave inversion results. *Earthquake Sci*, 37: 529–545
- Zhang X, Song X, Li J. 2022. A comparative study of seismic tomography models of the Chinese continental lithosphere. *Earthquake Sci*, 35: 161–185
- Zhang X, Song X, Wang F. 2023. A comparative study of seismic tomography models of Southwest China. *Earthquake Sci*, 36: 15–39
- Zhang Y, Gao Y. 2017. The characteristics of crustal shear-wave splitting in North-South seismic zone revealed by near field recordings of two observation periods of ChinArray (in Chinese). *Chin J Geophys*, 60: 2181–2199
- Zhang Z, Feng J, Yao H. 2023. 3-D azimuthal anisotropy structure reveals different deformation modes of the crust and upper mantle in the southeastern Tibetan Plateau. *Front Earth Sci*, 11: 1095609
- Zhao D, Hasegawa A, Horiuchi S. 1992. Tomographic imaging of P and S wave velocity structure beneath northeastern Japan. *J Geophys Res*, 97: 19909–19928
- Zhao D, Yu S, Liu X. 2016. Seismic anisotropy tomography: New insight into subduction dynamics. *Gondwana Res*, 33: 24–43
- Zheng T, Ding Z, Ning J, Chang L, Wang X, Kong F, Liu K H, Gao S S. 2018. Crustal azimuthal anisotropy beneath the southeastern Tibetan Plateau and its geodynamic implications. *J Geophys Res-Solid Earth*, 123: 9733–9749
- Zheng X F, Yao Z X, Liang J H, Zheng J. 2010. The role played and opportunities provided by IGP DMC of China National Seismic Network in Wenchuan earthquake disaster relief and researches. *Bull Seismol Soc Am*, 100: 2866–2872
- Zheng Y, Guo R. 2021. Earthquake potential of the seismic gap between the Wenchuan and Lushan earthquakes: Current status, thoughts, and challenges. *Sci China Earth Sci*, 64: 503–506